

LIGHT CURVE SIMULATION AND SHAPE INVERSION FOR HUMAN-MADE SPACE OBJECTS

by

Liam Robinson

A Thesis

Submitted to the Faculty of Purdue University

In Partial Fulfillment of the Requirements for the degree of

Master of Science in Aeronautics and Astronautics



School of Aeronautics and Astronautics

West Lafayette, Indiana

December 2023

**THE PURDUE UNIVERSITY GRADUATE SCHOOL
STATEMENT OF COMMITTEE APPROVAL**

Dr. Carolin Frueh

School of Aeronautics and Astronautics

Dr. Kenshiro Oguri

School of Aeronautics and Astronautics

Dr. Keith LeGrand

School of Aeronautics and Astronautics

Approved by:

Dr. Gregory Blaisdell

ACKNOWLEDGMENTS

I would like to thank my advisor, Dr. Carolin Frueh, for her guidance and mentorship. Her feedback has guided me through undergraduate research, publishing a conference paper, applying for fellowships, and now writing this thesis. For that, and her continued support through my PhD, I am forever grateful.

My friends and family have also been an amazing resource throughout my research. They've helped me workshop ideas, find bugs in code, and proofread proposals. Most importantly, they've always been willing to look at my unusual plots.

Finally, I must thank my committee, Dr. Oguri and Dr. LeGrand, for their feedback and attendance at my defense. Their comments have made this thesis what it is today.

This work was supported by Katalyst grant number FA6451-22-P-0019, Boeing work number SSOW-BRT-Z0722-5045, and the National Defense Science and Engineering Graduate Fellowship through the Air Force Office of Scientific Research under grant number FA9550-18-1-0154.

TABLE OF CONTENTS

LIST OF TABLES	7
LIST OF FIGURES	8
LIST OF SYMBOLS	10
ABSTRACT	12
1 Introduction	13
1.1 State of the Art	15
2 Light Curve Simulation	20
2.1 Attitude	20
2.1.1 Attitude Representations	20
The Direction Cosine Matrix	20
Principal Rotation Parameters	21
Quaternions	22
2.1.2 Attitude Kinematics	23
2.1.3 Attitude Dynamics	23
2.2 Computer Graphics	24
Camera Projections and Terminology	24
Transformations	25
2.3 Time Systems	27
2.3.1 Time Scales	28
2.3.2 Julian Date	29
2.3.3 Solar and Sidereal Time	30
2.4 Coordinate Systems	31
2.4.1 Latitude, Longitude and Altitude	31
Ellipsoid	31
Geoid	32

Terrain	33
Altitude Conversions	33
2.4.2 International Terrestrial Reference Frame (ITRF)	33
2.4.3 Topocentric Reference Frame (ENU)	35
2.4.4 International Celestial Reference Frame (ICRF/J2000)	36
2.4.5 Right Ascension and Declination	37
2.4.6 Azimuth and Elevation	38
2.4.7 Coordinate Transformations Summary	38
2.5 Photometry	39
2.5.1 The Charge Coupled Device (CCD)	39
2.5.2 Diffraction	39
Rayleigh Criterion	39
The Airy Disk	40
2.5.3 Signal-to-Noise Ratio (SNR)	42
2.5.4 Brightness Units	43
Irradiance	43
Apparent Magnitude	43
Normalized Irradiance	45
S_{10} Surface Brightness	45
Magnitude per Square Arcsecond	46
Candela	46
Photoelectron Counts	47
2.5.5 The Light Curve	48
2.6 CCD Performance Model	49
2.6.1 Background Signal Sources	50
Background Source Importance	50
Astronomical Spectra	51
Airglow	51
Light Pollution	52
Twilight	53

Integrated Starlight	55
Scattered Moonlight	57
Zodiacal Light	59
Background Sampling	60
2.6.2 Sensor Effects	62
Dark Noise	62
Readout Noise	63
Truncation Noise	63
3 Recommendations	64
4 Future Work	65
5 Appendices	66
5.1 Shadow Mapping	66
5.1.1 Shading	66
5.2 Astronomical Spectra Data	66
Atmospheric Extinction	66
5.2.1 Background Source Data	67
Lunar Phase Factor	67
Scattered Moonlight	67
Zodiacal Light	68
5.2.2 Telescope Parameters	69
Purdue Optical Ground Station	69
5.2.3 File Formats	69
Wavefront OBJ Example	69
REFERENCES	72

LIST OF TABLES

2.1	WGS-84 ellipsoid model of the Earth [3]	32
2.2	Background signal importance	50
5.1	Purdue Optical Ground Station telescope parameters	70

LIST OF FIGURES

1.1	Public tracked catalog in 2000 and 2023	14
2.1	Perspective and orthographic projections with relevant camera frustum attributes labeled	25
2.2	Time scales relative to TAI	29
2.3	EGM-96 geoid heights above the WGS-84 ellipsoid	32
2.4	MSL elevations surrounding the Purdue Optical Ground Station	33
2.5	ENU reference frame orientation at Purdue Optical Ground Station	36
2.6	Airy disk diffraction pattern	40
2.7	Signal-to-noise ratio reduction on a synthetic CCD pixel grid	42
2.8	Total solar irradiance variations at Earth and 1 AU. The solar cycle is apparent when distance is held constant at 1 AU, yielding small variations in the peak intensity at Earth.	44
2.9	Luminous efficiency function from [48]	47
2.10	Synthetic light curves in counts, irradiance, normalized irradiance, and apparent magnitude	49
2.11	Astronomical Spectra, atmospheric transmission and zero magnitude stellar spectrum from [9]	51
2.12	Airmass function comparison. The Van-Rhijn factor diverges to $+\infty$ while Pickering's function reaches the correct maximum of $AM(\theta_z) \approx 40$	53
2.13	Mean airglow signal on the local observer hemisphere. The observer is in New Mexico, USA at 32.900° N, -105.533° W	54
2.14	Zenith light pollution in the eastern USA, data from [50]	55
2.15	Mean light pollution signal on the local observer hemisphere. The observer is in New Mexico, USA at 32.900° N, -105.533° W	56
2.16	Twilight model surface brightness at zenith as a function of solar zenith angle	57
2.17	Mean twilight signal on the local observer hemisphere. The observer is in New Mexico, USA at 32.900° N, -105.533° W	58
2.18	Raw image of three GEO objects with stars streaking through the background. As expected the star signals have a variety of signal-to-noise ratios. Taken by the Purdue Optical Ground station at 32.900° N, -105.533° W by Nathan Houtz.	59
2.19	Integrated starlight brightness map	60

2.20 Integrated starlight signal on the local observer hemisphere. The observer is in New Mexico, USA at 32.900° N, -105.533° W	61
2.21 Mean scattered moonlight signal on the local observer hemisphere. The observer is in New Mexico, USA at 32.900° N, -105.533° W	62
2.22 Mean zodiacal light signal on the local observer hemisphere. The observer is in New Mexico, USA at 32.900° N, -105.533° W	63

LIST OF SYMBOLS

I	irradiance in $\left[\frac{W}{m^2}\right]$
\hat{I}	normalized irradiance in $[W]$
I_0	Irradiance of Vega $\left[\frac{W}{m^2}\right]$
m	Apparent magnitude [<i>nondim</i>]
JD	Julian date
T	Julian centuries
θ_{GMST}	Greenwich mean sidereal time
θ_r	Angular offset of the first zero of the Airy disk diffraction pattern
$C_{\text{Airy}}(\theta)$	CCD signal amplitude due to an Airy disk diffraction pattern [ADU]
k	Wavenumber
r_d	Telescope aperture radius [m]
d	Telescope aperture diameter [m]
A_{aperture}	Telescope aperture area [m^2]
f	Telescope focal length [m]
λ	Wavelength [m]
$FWHM$	Full width at half maximum
$C_{\text{Gauss}}(\theta)$	CCD signal amplitude due to a Gaussian approximation of the Airy disk [ADU]
$\text{STRINT}(\lambda)$	Representative zero apparent magnitude star irradiance spectrum $\left[\frac{W}{m^2 \cdot m}\right]$
$\text{QE}(\lambda)$	Quantum efficiency spectrum $\left[\frac{\text{ADU}}{m}\right]$
$\text{ATM}(\lambda)$	Atmospheric transmission spectrum $\left[\frac{1}{m}\right]$
$K_{cd}(\lambda)$	Luminous efficacy spectrum $\left[\frac{lm}{W}\right]$
SINT	CCD ADU conversion factor $\left[\frac{\text{ADU}}{W \cdot m^{-2} \cdot s}\right]$
$\text{SUN}(\lambda)$	Solar irradiance spectrum $\left[\frac{W}{m^2 \cdot m}\right]$
$\text{GLINT}(\lambda)$	Airglow radiance spectrum $\left[\frac{W}{m^2 \cdot m \cdot sr}\right]$
AINT	Intermediate airglow signal $\left[\frac{1}{s \cdot sr}\right]$
θ_z	Zenith angle [rad]
$\text{AM}(\theta_z)$	Relative airmass function [<i>nondim</i>]

s_{pix}	Telescope pixel scale $\left[\frac{arcsec}{pix} \right]$
Δt	CCD integration time [s]
$B_{poll,z}$	Zenith light pollution brightness in magnitudes per square arcsecond
$\bar{S}_{airglow}$	Mean airglow signal [ADU]
γ	Solar zenith angle [deg]
$B_{twi,z}$	Zenith twilight brightness in magnitudes per square arcsecond
$\bar{S}_{twilight}$	Mean twilight signal [ADU]
BINT	Zero magnitude starlight signal $\left[\frac{ADU}{s} \right]$
\bar{S}_{star}	Mean integrated starlight signal [ADU]
F_{rs}	Moonlight Rayleigh scattering radiance spectrum $\left[\frac{W}{m^2 \cdot m \cdot sr} \right]$
F_{ms}	Moonlight Mie scattering radiance spectrum $\left[\frac{W}{m^2 \cdot m \cdot sr} \right]$
F_{mt}	Total scattered moonlight radiance spectrum $\left[\frac{W}{m^2 \cdot m \cdot sr} \right]$
$f(\theta)$	Lunar brightness phase function [nondim]
\bar{S}_{moon}	Mean scattered moonlight signal [ADU]
\bar{S}_{zod}	Mean zodiacal light signal [ADU]
$\lambda_{background}$	Mean of background signal Poisson distribution [ADU]
\hat{n}	Face outward pointing unit normal vector
(v_1, v_2, v_3)	First, second, and third vertices $v_i \in \mathbb{R}^3$ on a given triangular face
h_i	Support of the ith face
\vec{E}	Extended Gaussian Image
f_r	Bidirectional Reflectance Distribution Function
L	Illumination direction unit vector
O	Observation direction unit vector
H	Halfway unit vector
C_d	Coefficient of diffuse reflection
C_s	Coefficient of specular reflection
C_a	Coeffieicnt of absorption
n	Specular exponent

ABSTRACT

Characterizing unknown space objects is an important component of robust space situational awareness. Estimating the shape of an object allows analysts to perform more accurate orbit propagation, probability of collision, and inference analysis about the object’s origin. Due to diffraction and atmospheric effects, most resident space objects of interest are unresolved when observed from the ground with electro-optical sensors. State of the art techniques for object characterization often rely on light curves — the time history of the object’s observed brightness. The brightness of the object is a function of the object’s shape, material properties, and attitude profile, along with the observation geometry. The process of recovering shape information from brightness measurements is known as the light curve shape inversion problem. This problem is ill-posed without further assumptions: modern direct shape inversion methods require that the attitude profile and material properties of the object is known, or at least can be hypothesized. This work describes improvements to light curve simulation and new methods for direct shape inversion for convex and nonconvex objects with realistic measurement noise. In particular, this work finds that improvements to the convex shape inversion process produce more accurate, sparser geometry in less time. The proposed nonconvex shape inversion method is effective at resolving singular large concave feature.

1. Introduction

Humankind has been creating space debris since the dawn of the space age [1]. Early missions like Vanguard 1, launched in March of 1958, set a precedent by leaving both their satellite and the launch vehicle’s upper stage in orbit, both of which are still in orbit in 2023 [2]. Vanguard was launched into Low Earth Orbit (LEO) — defined by the European Space Agency (ESA) as any orbit with an altitude below 2000 kilometers [1]. Above LEO lies Medium Earth Orbit (MEO) for orbital altitudes between 2000 and 31570 kilometers, and Geostationary Earth Orbit (GEO) between 35586 and 35986 kilometers altitude [1]. Half a century of increasingly frequent launches has created a space environment cluttered with thousands of debris objects, increasing the number of serious conjunction events that may require avoidance maneuvers for large satellites in LEO to over 100 during 2021 [1]. While very few mission-ending collisions are occurring on a yearly basis in the early 2020s, simulations predict over 200 catastrophic collisions per year if the trend in new launches and disposal practices continue [1]. This uncontrolled proliferation of human-made space debris puts space operations at risk. High-profile satellite collisions like Iridium-Cosmos in 2009 have added fuel to the fire, producing shells of debris that further pollute LEO [3]. Anti-satellite tests carried out by the USA, Russia, China, and India since the 1960s see nations destroying their own satellites, projecting military strength at the cost of creating more debris [3]. Beyond LEO in Geostationary Transfer Orbit (GTO), exploding launch vehicle upper stages produce large amounts of debris [1]. While higher orbits are not yet as polluted as LEO, they do not decay due to atmospheric drag, allowing debris objects to remain in the environment indefinitely [3].

In the context of the modern space environment, determining the current state and predicting the future dynamics of space objects is critical for many areas of Space Domain Awareness (SDA) [4]. While the current orbits of objects can be determined accurately from astrometry — through passive optical imagery or active radar — their future dynamics are perturbed by non-conservative forces driven by their shape, attitude profile, and material properties that cannot be observed directly. In particular, objects in orbits with altitudes higher than LEO are most efficiently observed with optical telescopes as the power required

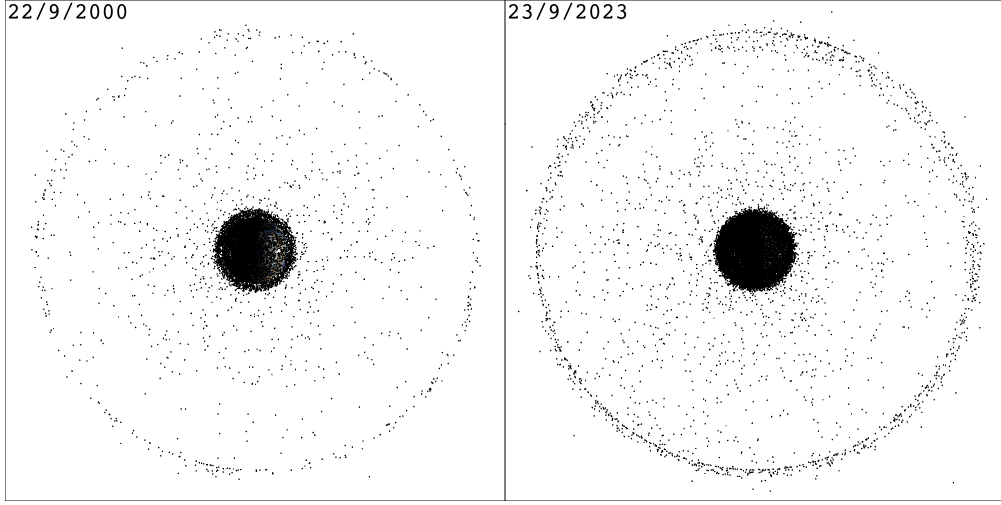


Figure 1.1. Public tracked catalog in 2000 and 2023

for radar scales with the square of the distance [4]. Because optical observations are already commonly used to characterize the orbit of the objects in orbits past LEO, it is advantageous to use the same existing sensors — or in some cases even the same images — to extract these other useful characteristics.

Characterizing an object’s shape, attitude, and material properties is fundamentally difficult as distance from the sensor and atmospheric turbulence leaves only a distribution of brightness in the image [5]. The leftover information is the total brightness of the object, and this value over time is known as the light curve. Optical brightness observations are fundamentally limited by background and sensor noise [4]. Light curves are computed from observed optical data by estimating the background mean of the image, identifying which pixels of the image likely belong to the object, subtracting the mean background level from those pixels, and calibrating the remaining object signal using known stars elsewhere in the image [6]. Each images must also be monitored for contamination from background stars and over- and under-exposures [7]. Despite these realities, the light curve is a function of the parameters of interest: the object’s shape, attitude, and material properties [5], [8]. Solving light curve shape inversion in a general case would enable robust active debris removal,

anomaly detection, and collision avoidance, all of which are benefitted by accurate shape information.

Due to the environmental noise and fundamental physical limitations on the processes driving the light curve, the measured brightness is dependent on the overall brightness and hence varies from data point to data point in the light curve. Furthermore, given the Poisson nature of the light collection process, a constant Gaussian assumption of the measurement noise in the light curve may not be suitable [5], [9]. A realistic representation of the light curve can only be achieved by accounting for the physical processes simulating the lighting and measurement process, followed by the measurement reduction and correction processing steps.

1.1 State of the Art

Light curve shape inversion was first investigated by Russell in 1906, who proposed a spherical harmonic representation that could be fit to an asteroid shape [10]. Russell noted that there would be ambiguity in the shape solution such that many solutions would fit the data equally well. The next major contribution to the field was due to Kaasalainen and Torppa in 2000, who successfully reconstructed the shapes of asteroids by directly optimizing the directions and areas of candidate faces — encapsulated by the so-called Extended Gaussian Image (EGI) — to find a convex shape that produces a similar light curve [11], [12]. Once the EGI is estimated, Kaasalainen and Torppa recover the vertices and faces of the corresponding convex object using a result of Minkowski and a nonlinear, convex optimization problem implemented by Little [13], [14]. Any EGI-based method in the asteroid or human-made object shape inversion literature uses some variation of this final stage to reconstruct the final estimated geometry. Kaasalainen and Torppa also addressed nonconvex shape inversion by optimizing a spherical harmonics shape representation to reconstruct the largest nonconvex features of an asteroid, noting that smoothness regularization was sometimes needed to prevent the shape from degenerating [11]. In the work of Kaasalainen and Torppa, the EGI optimization takes place in a single step as the asteroid shapes under study do not have sparse EGIs. By contrast, this work introduces stages that increase shape accu-

racy and lower computation time by leveraging the natural sparsity of human-made objects. Durech and Kaasalainen extended on this work in 2003 by investigating the observability of nonconvex features in asteroid light curves, finding that concave features are often observable only at high phase angles, supporting the conclusion that robust nonconvex shape inversion requires very different considerations than its convex counterpart [15]. In 2022, Chng et al. proposed a method to determine a optimal spin pole and convex shape via the EGI, offering computational benefits over Kaasalainen and Torppa while guaranteeing global optimality in the solution with respect to the input brightness data, while being limited to convex shape estimates[16]. Using the methods originally proposed by Kaasalainen and Torppa, a collaborative effort of dozens of observatories lead to the publication of Database of Asteroid Models from Inversion Techniques (DAMIT), a publicly-available repository of convex asteroid models [17]. As of October 2023, DAMIT currently hosts 16,086 models for 10,751 asteroids [18].

Shape inversion for human-made space objects differs from the asteroid inversion in a few important aspects. More diverse methods exist, being generally segmented into EGI-based methods drawing from the asteroid literature, filter-based methods for simultaneous attitude and shape solutions, and machine learning for classifying object shape from the light curve. Due to the increased number of unknowns in the material properties and attitude profile when observing an arbitrary human-made object, the inverted light curves are often simulated as part of the same work. This highlights the importance of realistic light curve simulation to effectively test proposed inversion methods.

Direct shape inversion for human-made space objects was first investigated by Calef et al., who adopted Kaasalainen and Torppa’s methods applied to multispectrum measurements to reduce the ambiguities of the different material properties common in human-made objects [19]. Bradley and Axelrad also used asteroid inversion techniques to recover convex approximations of CubeSats, rocket bodies, and box-wing satellites using the inversion codes developed and released by Kaasalainen, yielding good results for rocket body-like shapes but limited success for box-wing satellites and other high area-to-mass ratio (HAMR) objects [20]. The most recent major contributions to the direct shape inversion literature are due to Fan and Frueh, inverted the shape of convex human-made objects from noisy light curves

using the EGI with a multi-hypothesis scheme to reduce the ambiguity introduced by noisy measurements [5], [21], [22]. Fan notes that full observability is crucial for successful direct shape inversion, pointing to work by Friedman and Frueh, who quantified the observability of EGI inversion to inform sensor tasking schemes [23], [24]. Cabrera et al. applied area regularization to Fan and Friedman’s methods, achieving more accurate convex shape estimates and finding that natural constraints on the EGI area optimization renders the problem estimatable before it becomes classically observable [25]. Throughout the shape inversion literature, two themes are clear. Effective and efficient methods for nonconvex shape inversion for human-made objects are needed, and existing convex inversion methods have not been designed to work with realistic measurement noise. This work seeks to address both of these challenges by presenting a method for inverting large singular concave features in addition to a scheme for robustly inverting convex and nonconvex shapes with physically-based measurement noise.

Outside of the asteroid-inspired EGI methods, the literature falls into two broad categories: filter-based inversion, and machine learning categorization. Each offers different advantages while imposing unique limitations. Filter-based shape inversion was been pioneered by Linares through work with various co-authors. These filter-based methods often seek to perform multiple types of object characterization simultaneously, estimating attitude and material properties in addition to shape [26]–[28]. Because the input data for filter-based approaches is still only unresolved brightness measurements, estimating more properties in an already ill-posed problem requires a loss of fidelity in the solution elsewhere. Often, the shape model is highly simplified to make the problem more tractable [26]–[28]. Linares et al. have implemented unscented Kalman filters [26], multiple-model adaptive estimation algorithms [27], and adaptive Hamiltonian Markov chain Monte Carlo schemes [28] which achieve good results for simple shapes, but have not been tested on complex and realistic geometries [28]. In general, filter-based approaches are limited by the nonlinearity of highly specular and complex human-made objects, but require less information to run. Direct inversion methods that use the EGI require more *a priori* information, but are able to deliver more accurate shape estimates.

By contrast, machine learning categorization methods indirectly recover shape information by predicting which class of objects an observed light curve belongs to. Linares and Furfaro used a deep convolutional neural network to classify novel light curves as rocket bodies, payloads, or debris, achieving good classification accuracy at the cost of uncertainty about how the model would behave for light curves collected for objects outside of its training dataset [29]. Other authors, including Kerr et al. and McNally et al. have adapted the architecture developed by Furfaro et al. to classify novel light curves into an extended set of object types, demonstrating that these models are flexible enough to differentiate between many object types and attitude profiles, although with higher error rates [30], [31]. Allworth et al. applied transfer learning to classify real measurements using a synthetically-trained model, supporting the applicability of these approaches to operational decision-making [32].

There has also been significant work published on extracting light curves of human-made objects from real optical observations. Schildknecht et al. used color photometry to investigate isolate material properties of high area-to-mass ratio (HAMR) objects in GEO [6]. Karpov et al. used wide-field monitoring system to collect light curves from LEO objects [33]. Benson et al. collected light curves from retired GOES, Inmarsat, and Astra satellites in geosynchronous orbit to characterize their spin states [34]. Koshkin et al. collected light curves of TOPEX/Poseidon, among other inactive satellites, to determine their spin poles and rates [35]. Wang et al. collected light curves from GOES-8, an active GEO satellite, and simulated material properties and attitude profile to attribute peaks in its observed brightness to different parts of the spacecraft [36].

The state of the art in light curve simulation differs between approaches and the object class under study. Kaasalainen and Torppa, as well Fan, Friedman, Kobayashi, and Frueh employ a Lambertian model for convex objects with a facetwise ray tracing scheme for nonconvex objects [5], [12], [23], [37]–[39]. This approach has the advantage of being simple, but can be computationally intensive for complex objects. Allworth et al. developed a ray traced light curve simulator in based on Blender’s cycles renderer, allowing them to account for photorealistic shadowing and motion blur [32], [40]. Furfaro et al. [41] and Cabrera and Bradley [20], [25] use a simple Lambertian model with no self-shadowing. Many more authors apply a more specialized non-Lambertian Bidirectional Reflectance Distribution Function

(BRDF) for their lighting [28], [31], [42]. Throughout the literature, there is a clear gap between the simulated light curves and their observed counterparts. Due to the difference in quality, authors often treat real and simulated data very differently [32]. This work presents a physically-based lighting, shadowing, and noise model to produce synthetic light curves of similar quality to observed data, enabling more robust validation of the presented inversion techniques.

2. Light Curve Simulation

Light curve simulation and inversion requires background knowledge in attitude kinematics, time and coordinate systems, computer graphics, and photometry.

2.1 Attitude

In order to effectively compute reflections and shadows on the surfaces of space objects, that object must have an assigned orientation in inertial space. While defunct satellites and space debris are slowly spun up by the Yarkovsky-O'Keefe-Radzievskii-Paddack (YORP) effect, the short-term motion of non-operational space objects is well-approximated by torque-free motion [43]. Developing the kinematics of torque-free motion first requires an understanding of common kinematic representations of orientation.

2.1.1 Attitude Representations

When discussing about the orientation of a rigid body in three dimensions, otherwise known as its attitude, that orientation is implicitly understood to be relative to some other reference frame. The direction of a unit vector can be expressed with two numbers — the azimuth and elevation of that vector. Naïvely, this could be extrapolated to conclude that six numbers are needed to express an orientation. Because the basis vectors form an orthonormal set $\{\hat{b}_1, \hat{b}_2, \hat{b}_3\}$, it follows for a right-handed system that $\hat{b}_3 = \hat{b}_1 \times \hat{b}_2$, $\hat{b}_2 = \hat{b}_3 \times \hat{b}_1$, and $\hat{b}_1 = \hat{b}_2 \times \hat{b}_3$. Each of these equations constrains one further degree of freedom, revealing that a minimum of three quantities are necessary to express the relative orientation of two reference frames. This minimum bound does not make any statements about the usefulness of three element sets; at least four dimensions are needed to remove singularities.

The Direction Cosine Matrix

The direction cosine matrix (DCM) is a 3×3 symmetric, orthogonal matrix, expressing the three basis vectors of one frame in another. This amounts to projecting each basis vector in the initial frame onto each basis vector of the final frame; the cosine of the angle between

the compared vectors. It is notated with two capital letters, the rightmost indicating the reference frame of the input vectors and the leftmost indicating the transformed frame. Alternatively, the DCM is sometimes expressed as C when the frames involved are arbitrary or do not need to be denoted. For example, the DCM $[\mathcal{BN}]$ takes a vector ${}^N\mathbf{r}$ in the \mathcal{N} frame to the \mathcal{B} frame as ${}^B\mathbf{r}$:

$${}^B\mathbf{r} = [\mathcal{BN}] {}^N\mathbf{r}. \quad (2.1)$$

The orthogonal property of the DCM implies $[\mathcal{BN}]^{-1} = [\mathcal{BN}]^T$ such that $[\mathcal{BN}]^T = [\mathcal{N}\mathcal{B}]$.

Principal Rotation Parameters

Another common attitude representation is the Euler angle-axis set, otherwise known as principal rotation parameters [44]. Euler's rotation theorem guarantees that any relative orientation can be expressed as a single rotation about an axis $\hat{\lambda} \in \mathbb{S}^2$ by an angle $\theta \in [0, 2\pi]$ [44]. The set $\{\hat{\lambda}, \theta\}$ is known as a principal rotation parameter, abbreviated PRP hereafter. The DCM is mapped to the PRP representation with:

$$\begin{aligned} \theta &= \cos^{-1} \left(\frac{1}{2} [C_{1,1} + C_{2,2} + C_{3,3} - 1] \right), \\ \hat{\lambda} &= \frac{1}{2 \sin \theta} \begin{bmatrix} C_{2,3} - C_{3,2} \\ C_{3,1} - C_{1,3} \\ C_{1,2} - C_{2,1} \end{bmatrix}, \end{aligned} \quad (2.2)$$

where $C_{i,j}$ refers to the i th row and j th column of C [45]. The mapping from PRP to DCM is also relatively straightforward:

$$C = I_3 + \sin \theta [\hat{\lambda} \times] + (1 - \cos \theta) [\hat{\lambda} \times]^2, \quad (2.3)$$

where $[v \times]$ is the matrix cross product operator, defined on $\mathbf{v} \in \mathbb{R}^3$ as:

$$[\mathbf{v} \times] = \begin{bmatrix} 0 & -v_3 & v_2 \\ v_3 & 0 & -v_1 \\ -v_2 & v_1 & 0 \end{bmatrix}. \quad (2.4)$$

This operator is useful as it rephrases the cross product as matrix multiplication, i.e. $\mathbf{v} \times \mathbf{u} = [\mathbf{v} \times] \mathbf{u}$. While the PRP $\{\theta, \hat{\lambda}\}$ is a four element set, there are only three degrees of freedom due to the unit norm constraint on $\hat{\lambda}$.

Quaternions

The quaternion represents attitude with a point on the surface of the hypersphere \mathbb{S}^3 . In terms of the PRP, the quaternion is given by [44]:

$$\mathbf{q} = \begin{bmatrix} \hat{\lambda} \sin(\theta) \\ \cos(\theta) \end{bmatrix}. \quad (2.5)$$

The first three entries of the quaternion are often called the vector component, with the final entry being the scalar component. Some authors reorder the quaternion, placing the scalar term first. Often the entries of a single quaternion are referenced by index such that $\mathbf{q} = [q_1, q_2, q_3, q_4]$. Similarly, the vector portion of the quaternion is referenced with $\mathbf{q}_{1:3}$. The quaternion can be mapped back to the PRP [44] via

$$\begin{aligned} \theta &= \cos^{-1}(q_4) \\ \lambda &= \frac{\mathbf{q}_{1:3}}{\sin \theta}. \end{aligned} \quad (2.6)$$

The quaternion maps to the DCM [44] via

$$C = \begin{bmatrix} -q_2^2 - q_3^2 + q_1^2 + q_4^2 & 2q_1q_2 + 2q_3q_4 & 2q_1q_3 - 2q_2q_4 \\ 2q_1q_2 - 2q_3q_4 & -q_1^2 - q_3^2 + q_2^2 + q_4^2 & 2q_1q_4 + 2q_2q_3 \\ 2q_1q_3 + 2q_2q_4 & 2q_2q_3 - 2q_1q_4 & -q_1^2 - q_2^2 + q_3^2 + q_4^2 \end{bmatrix} = \Xi(q)^T \Psi(q). \quad (2.7)$$

In Eq 2.7, Ψ is defined to be [44]

$$\Psi = \begin{bmatrix} q_4 & q_3 & -q_2 \\ -q_3 & q_4 & q_1 \\ q_2 & -q_1 & q_4 \\ -q_1 & -q_2 & -q_3 \end{bmatrix}. \quad (2.8)$$

2.1.2 Attitude Kinematics

Because it is cheap to convert between attitude representations, only one set of kinematic equations are needed for propagating a rigid body attitude profile from an initial condition. Quaternion kinematic differential equations are chosen as they have no singularity and produce very smooth dynamics that are easy to integrate when compared to three-variable representations that possess singularities. Given the current orientation quaternion $\mathbf{q} = [q_1, q_2, q_3, q_4]^T$ and angular velocity $\omega = [\omega_1, \omega_2, \omega_3]^T$ the quaternion derivative is computed via:

$$\begin{bmatrix} \dot{\epsilon}_1 \\ \dot{\epsilon}_2 \\ \dot{\epsilon}_3 \\ \dot{\epsilon}_4 \end{bmatrix} = \frac{1}{2} \begin{bmatrix} \epsilon_4 & -\epsilon_3 & \epsilon_2 & \epsilon_1 \\ \epsilon_3 & \epsilon_4 & -\epsilon_1 & \epsilon_2 \\ -\epsilon_2 & \epsilon_1 & \epsilon_4 & \epsilon_3 \\ -\epsilon_1 & -\epsilon_2 & -\epsilon_3 & \epsilon_4 \end{bmatrix} \begin{bmatrix} \omega_1 \\ \omega_2 \\ \omega_3 \\ 0 \end{bmatrix}. \quad (2.9)$$

2.1.3 Attitude Dynamics

Rigid body dynamics can be easily expressed in the body principal axes with an arbitrary torque $\mathbf{M} = [M_1, M_2, M_3]^T$ in the same frame via:

$$\begin{bmatrix} \dot{\omega}_1 \\ \dot{\omega}_2 \\ \dot{\omega}_3 \end{bmatrix} = \begin{bmatrix} (M_1 + I_2\omega_2\omega_3 - I_3\omega_2\omega_3) / I_1 \\ (M_2 - I_1\omega_1\omega_3 + I_3\omega_1\omega_3) / I_2 \\ (M_3 + I_1\omega_1\omega_2 - I_2\omega_1\omega_2) / I_3 \end{bmatrix}. \quad (2.10)$$

Equations 2.10 and 2.9 are numerically integrated to yield the orientation time history which is necessary for later light curve simulations. Often, $\mathbf{M} = \mathbf{0}$ is chosen to simulate the torque-free evolution of an initial orientation and spin state, neglecting small attitude perturbations over the simulation interval.

2.2 Computer Graphics

The light curve simulation framework developed in this work relies on a pixel-by-pixel image rendering on the GPU to compute the total reflected irradiance at each timestep of the simulation. As a result, a background in common computer graphics terminology and reference frames is necessary to understand the transformation from coordinates in the object body frame to a pixel in the final image.

Camera Projections and Terminology

In computer graphics, a camera is defined by its position R_{cam} , target T_{cam} , reference up direction U_{cam} , and a field of view FOV . In order to render a 3D scene to a 2D image using this camera, a transformation is needed. An orthographic camera accomplishes this transformation by orthogonally projecting points onto a plane perpendicular to camera look direction $T_{cam} - R_{cam}$. The volume of space that falls into view of the camera is known as the frustum [46]. An important consequence of orthogonal projection is that objects further away from the camera do not shrink in the image, which is sometimes advantageous. A perspective projection forms a more complex frustum that expands outwards from a near plane to a proportionally larger far plane. Because of the expansion of the frustum, geometry processed by the perspective transformation shrinks as it moves further from the near plane. Figure 2.1 displays the geometry of these camera frustums, with additional reference frames detailed in Section 2.2.

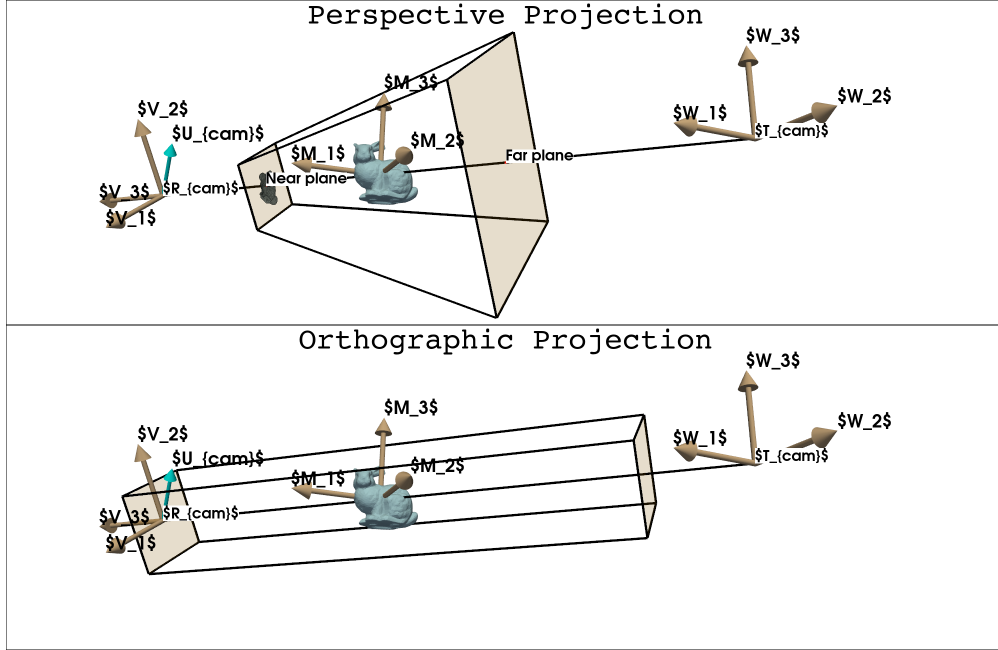


Figure 2.1. Perspective and orthographic projections with relevant camera frustum attributes labeled

Transformations

Transformations in computer graphics are often represented by 4×4 matrices. These matrices operate on so-called homogeneous coordinates, operating on vectors in \mathbb{R}^4 of the form $[x, y, z, w]^T$ [46]. The inclusion of the fourth component enables simultaneous rotation, translation, and scaling of the input points by the matrix, provided that the outputs are normalized to set $w = 1$ [46].

There are a few fundamental matrices used in computer graphics that are necessary for later hardware-accelerated light curve simulation algorithms. The first is the model matrix $M \in \mathbb{R}^{4 \times 4}$ which transforms from the world frame to the model frame given the origin of the model body frame $R_m \in \mathbb{R}^{3 \times 3}$ and the orientation of the model body frame relative to the world frame $\mathbf{q}_m \in \mathbb{R}^4$ as a quaternion [46]:

$$M = \begin{bmatrix} -q_2^2 - q_3^2 + q_1^2 + q_4^2 & 2q_1q_2 + 2q_3q_4 & 2q_1q_3 - 2q_2q_4 & -R_{m,x} \\ 2q_1q_2 - 2q_3q_4 & -q_1^2 - q_3^2 + q_2^2 + q_4^2 & 2q_1q_4 + 2q_2q_3 & -R_{m,y} \\ 2q_1q_3 + 2q_2q_4 & 2q_2q_3 - 2q_1q_4 & -q_1^2 - q_2^2 + q_3^2 + q_4^2 & -R_{m,z} \\ 0 & 0 & 0 & 1 \end{bmatrix}. \quad (2.11)$$

Eq 2.11 uses Eq 2.7 to transform the quaternion into a DCM. The model matrix basis vectors are illustrated in Figure 2.1 as M_i , with the world frame basis vectors notated with W_i . Given the location of the camera origin $R_{cam} \in \mathbb{R}^3$, its target position $T_{cam} \in \mathbb{R}^3$, and the camera up direction $U_{cam} \in \mathbb{R}^3$, the view matrix $V \in \mathbb{R}^{4 \times 4}$ that transforms from the world frame to the camera frame is given by [46]:

$$v_3 = \frac{R_{cam} - T_{cam}}{\|R_{cam} - T_{cam}\|} \quad (2.12)$$

$$v_1 = \frac{U_{cam} \times v_3}{\|U_{cam} \times v_3\|}$$

$$v_2 = v_1 \times v_3$$

$$V = \begin{bmatrix} v_{1,x} & v_{1,y} & v_{1,z} & -v_1 \cdot R_{cam} \\ v_{2,x} & v_{2,y} & v_{2,z} & -v_2 \cdot R_{cam} \\ v_{3,x} & v_{3,y} & v_{3,z} & -v_3 \cdot R_{cam} \\ 0 & 0 & 0 & 1 \end{bmatrix}.$$

The view matrix basis vectors are illustrated in Figure 2.1 as V_i . Given the field of view of the camera FOV in radians, the distance from the camera origin to the near n and far f clipping planes, and the camera aspect ratio a , the orthographic projection matrix $P \in \mathbb{R}^{4 \times 4}$ that transforms from the camera frame to the image plane is given by [46]:

$$t = n \cdot \tan\left(\frac{FOV}{2}\right) \quad (2.13)$$

$$r = t \cdot a$$

$$P = \begin{bmatrix} \frac{2n}{2r} & 0 & 0 & 0 \\ 0 & \frac{2n}{2t} & 0 & 0 \\ 0 & 0 & -\frac{f+n}{f-n} & \frac{2fn}{f-n} \\ 0 & 0 & -1 & 0 \end{bmatrix}$$

Together, these matrices form the so-called Model-View-Projection matrix which transforms directly from coordinates in the object body frame r_{obj} to the image plane:

$$\begin{bmatrix} x_h \\ y_h \\ z_h \\ w_h \end{bmatrix} = MVP \begin{bmatrix} r_{obj,x} \\ r_{obj,y} \\ r_{obj,z} \\ 1 \end{bmatrix}. \quad (2.14)$$

In Eq 2.14, x_h/w_h and y_h/w_h are homogeneous coordinates in the image plane, running linearly from $[-1, -1]$ at the top left corner of the image to $[1, 1]$ at the bottom right. Given the width of the image in w_{pix} pixels, the image coordinates (x, y) of r_{obj} in pixels are:

$$\begin{bmatrix} x \\ y \end{bmatrix} = \begin{bmatrix} w_{pix} \left(\frac{1}{2} + \frac{x_h}{2w_h} \right) \\ a \cdot w_{pix} \left(\frac{1}{2} + \frac{y_h}{2w_h} \right) \end{bmatrix}. \quad (2.15)$$

The transformation summarized in Eqs 2.14 and 2.15 are crucial in Section ?? for the shadow mapping algorithm used to compute pixel-wise self-shadowing effects.

2.3 Time Systems

In order to accurately predict the position of a space object and an observer, it is necessary to understand how a given time translates to the orientation of the relevant reference frames.

These calculations require conversions between various time scales, the Julian date, and sidereal time.

2.3.1 Time Scales

There are a variety of scales used to measure time. What follows is a minimal treatment of each. For a more comprehensive overview, see Section 3.5 of [3]. International Atomic Time (TAI) is based on measurements from atomic clocks and is independent of astronomical effects or observations. By definition, TAI proceeds at the rate of 1 SI second per second. Universal Time (UT0) is derived directly from observations of the apparent position of the stars. UT1 is derived from UT0 by adjusting for polar motion. UT1 is offset from TAI by $\Delta UT1$, which is a dynamic quantity that must be continually observed. Universal Coordinated Time (UTC) is a truncation of UT1 that uses an integer number of leap seconds ΔAT to stay within 0.9 seconds of TAI. Terrestrial Time (TT) is defined by a constant offset of $TT - TAI = 32.184$ seconds from TAI and proceeding at the same rate as TAI. These time scale relations are summarized in Eq 2.16.

$$UTC = UT1 - \Delta UT1 \tag{2.16}$$

$$TAI = UTC + \Delta AT$$

$$TT = TAI + 32.184^s$$

These time scales are relevant for this research as the precise coordinate frame transformation from ITRF to the J2000.0 realization of ICRF relies on quantities expressed in UT1. Date timestamps are usually standardized to UTC, requiring the transformations in Eq 2.16 for full accuracy. Figure 2.2 shows the evolution of UTC, UT1, and TT with respect to TAI. Notice that $\Delta UT1$ continually changes while ΔAT is always truncated to a nearby integer.

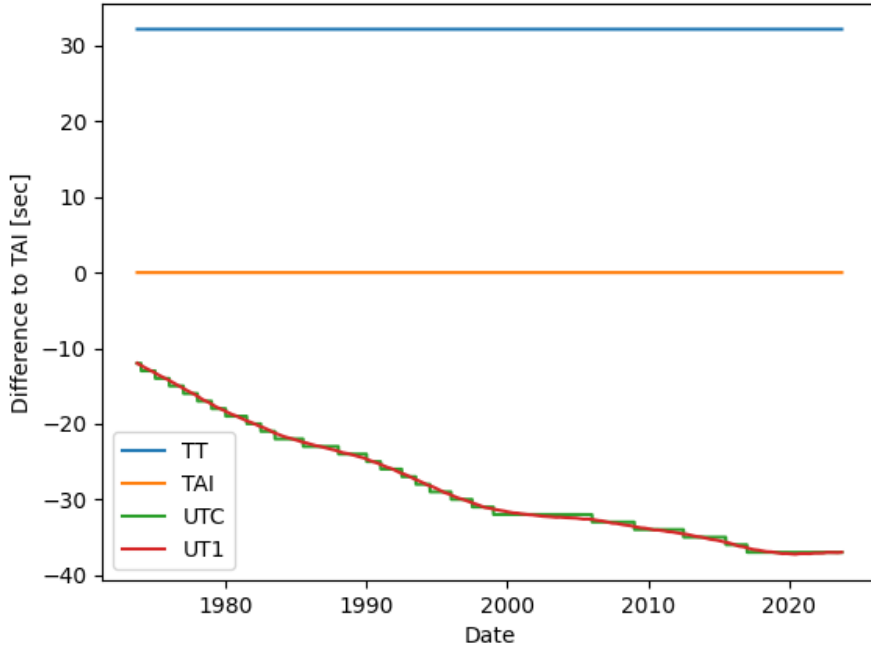


Figure 2.2. Time scales relative to TAI

2.3.2 Julian Date

Most tasks in astrodynamics are easier when using a continuous time system. For this reason, the Julian date is adopted. This quantity is defined as the number of days elapsed since January 1, 4713 B.C., at 12:00 [3]. Given a date timestamp of the form D/M/Y h:m:s between the years of 1900 and 2100, the Julian date is computed via:

$$JD = 376Y - \text{floor} \left[\frac{7Y + 7 \cdot \text{floor} \left(\frac{M+9}{12} \right)}{4} \right] + \text{floor} \left(\frac{275M}{9} \right) + d + 1721013.5 + \frac{\frac{(s+60)}{60} + h}{24}. \quad (2.17)$$

Note that Eq 2.17 is always a function of the time scale used in the input, i.e., a UTC timestamp yields JD_{UTC} whereas a UT1 timestamp yields JD_{UT1} . Another useful quantity

for later time and coordinate system calculations is the number of Julian centuries since a particular epoch. The J2000.0 epoch is used unless otherwise stated, resulting in [3]:

$$T = \frac{JD - 2451545.0}{36535}. \quad (2.18)$$

Often, more specificity is needed with respect to the time scale used in Eq 2.18. For example, computing T with an input date in UT1 yields T_{UT1} using JD_{UT1} , which is in turn a function a date timestamp expressed in UT1.

2.3.3 Solar and Sidereal Time

A solar day is defined as the time required for the Sun to pass and return to an observer's meridian — a line of constant longitude extending from the geographic south pole to the geographic north pole [3]. By contrast, a sidereal day is the time required for the stars to complete a revolution around an observer's meridian. Due to the Earth's orbit around the Sun, the sidereal day is about 4 minutes shorter than the solar day [3]. The Greenwich mean sidereal time (GMST) is computed in seconds via [4]:

$$\theta_{GMST} = 67310.54841 + (3.15576 \cdot 10^9 + 8640184.812866) T_{UT1} + 0.093104 T_{UT1}^2 - 6.2 \cdot 10^{-6} T_{UT1}^3. \quad (2.19)$$

Accounting for the variations in the inclination of the ecliptic ϵ and the the change in the equinox compared to the reference epoch $\Delta\Psi$ produces Greenwich apparent sidereal time (GAST) via [4]:

$$\theta_{GAST} = \theta_{GMST} + \Delta\Psi \cos \epsilon. \quad (2.20)$$

Both the inclination of the ecliptic and the difference in the equinox are computed with series expansions following the IAU 1980 theory of nutation [3].

2.4 Coordinate Systems

A precise definition of coordinate systems is necessary for determining the position of the observer and the observed space object at a given time. The relevant conversions are summarized by a single question: how is a fixed position on the surface of the Earth transformed into a standardized inertial reference frame?

2.4.1 Latitude, Longitude and Altitude

Latitude, longitude, and altitude (LLA) are a spherical coordinates representation of position on or above the surface of the Earth. For the purposes of precise station positioning, the difference between the two types of longitude — geocentric and geodetic — is important. Geocentric latitude is the angle between the line from the center of mass of the Earth to the position of interest and the equatorial plane. Geodetic latitude instead measures the angle between the local ellipsoid surface normal and the equatorial plane. Geodetic latitude ϕ_{geod} is converted to geocentric ϕ_{geoc} latitude with [4]:

$$\phi_{geoc} = \tan^{-1} \left((1 - f)^2 \tan \phi_{geod} \right). \quad (2.21)$$

Additionally, the radius of the ellipsoid r_E at a given geocentric latitude is necessary for later conversion, expressed by [4]:

$$r_E = R_E - f \sin^2(\phi_{geoc}). \quad (2.22)$$

The altitude in an set of LLA coordinates needs a reference point. Different observers may be defined differently — either relative to the approximate ellipsoidal shape of the Earth, the hypothetical mean sea level, or the surrounding terrain.

Ellipsoid

Due to Earth's equatorial bulge, it is common to model the rough shape of the Earth as an ellipsoid. In particular, the 1984 World Geodetic Survey (WGS-84) model is used

throughout this work to define the shape of the Earth ellipsoid, with parameters listed in Table 2.1 for use in Eqs 2.21 and 2.22.

Parameter	Value
Equatorial radius R_E	6378.137 [km]
Flattening ratio f	1/298.257

Table 2.1. WGS-84 ellipsoid model of the Earth [3]

These parameters are needed for the conversion from LLA to the International Terrestrial Reference Frame.

Geoid

The geoid accounts for the gravitational potential differences across the Earth's surface [3]. It is a surface of equal gravitational potential; the surface the ocean relaxes to without the influence of the wind and tides [3]. For this reason, the geoid is alternatively known as the mean sea level (MSL). The ellipsoid is a good approximation of the geoid, which deviates from the ellipsoid by less than ≈ 100 meters at all latitudes and longitudes. The height of the geoid above the ellipsoid can be computed from a high-fidelity gravity model, but it is often more convenient to interpolate a pre-computed grid of geoid heights. Figure 2.3 displays global geoid heights derived from the 1996 Earth Gravitational Model (EGM-96) relative to the ellipsoid.

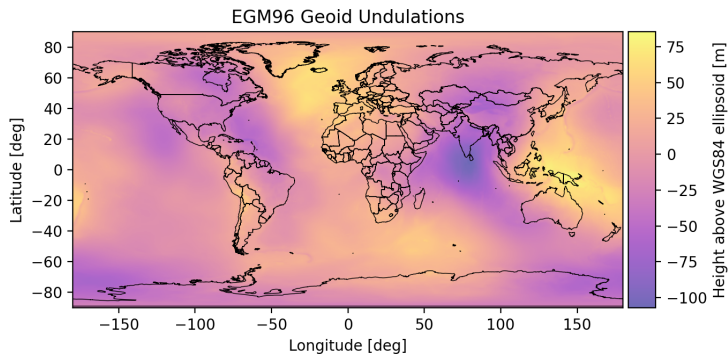


Figure 2.3. EGM-96 geoid heights above the WGS-84 ellipsoid

Terrain

Terrain elevation is usually the final component needed to fully define the altitude of a ground station, which is often defined relative to MSL. This work uses 30-meter terrain tiles from the Shuttle Radar Topography Mission (SRTM). Figure 2.4 shows the local elevation around the Purdue Optical Ground Station using SRTM data.

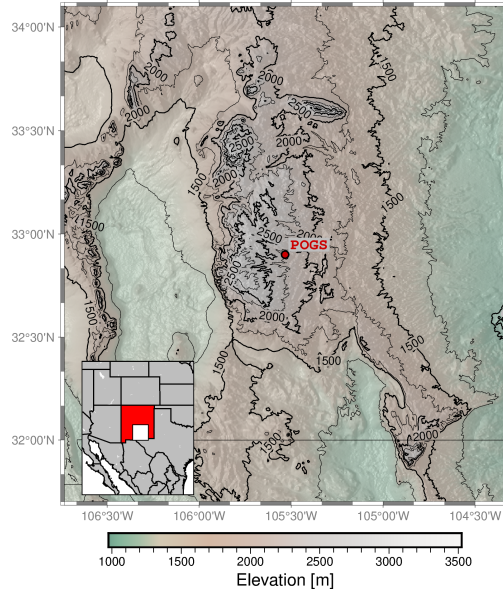


Figure 2.4. MSL elevations surrounding the Purdue Optical Ground Station

Altitude Conversions

Given an altitude relative to the terrain a_{terrain} , the elevation above the ellipsoid a_{ellip} is given as a function of the terrain elevation above the geoid $h_{\text{terrain}}(\lambda, \phi)$ and the geoid elevation above the ellipsoid $h_{\text{geoid}}(\lambda, \phi)$ by:

$$a_{\text{ellip}} = a_{\text{terrain}} + h_{\text{terrain}}(\lambda, \phi_{\text{geod}}) + h_{\text{geoid}}(\lambda, \phi_{\text{geod}}). \quad (2.23)$$

2.4.2 International Terrestrial Reference Frame (ITRF)

The cartesian form of LLA is known as the Earth-centered Earth-fixed (ECEF) reference frame. Throughout this work, ECEF and ITRF will be used interchangeably. This frame has

its origin at the center of mass of the Earth and its axes fixed in the crust. The fundamental plane of the frame is defined to be the equator — orienting the z -axis through Earth's instantaneous spin axis, and the reference direction through the intersection of the prime meridian and the equator — defining the x -axis. Completing the right-handed system with $\hat{y} = \hat{z} \times \hat{x}$ yields a reference frame that remains fixed, neglecting effects like continental drift. The transformation from LLA $(\lambda, \phi_{geod}, a_{ellip})$ to ITRF is given by Eq 2.24.

$$e^2 = 2f - f^2 \quad (2.24)$$

$$N = \frac{R_E}{\sqrt{(1 - e^2 \sin(\phi_{geod}))^2}}$$

$$\rho = (N + a_{ellip}) \cos(\phi_{geod})$$

$$x_{itr} = \rho \cos(\lambda)$$

$$y_{itr} = \rho \sin(\lambda)$$

$$z_{itr} = (N(1 - e^2) + a_{ellip}) \sin(\phi_{geod})$$

In Eq 2.24, e^2 is the squared eccentricity of the ellipsoid, N is the radius of curvature in the meridian, and ρ is the $x - y$ plane magnitude of the station's position [3].

Many later transformations require the body axis rotation matrices R_1 , R_2 , and R_3 which are expressed in Eq 2.25.

$$\begin{aligned}
R_1(\theta) &= \begin{bmatrix} 1 & 0 & 0 \\ 0 & \cos \theta & \sin \theta \\ 0 & -\sin \theta & \cos \theta \end{bmatrix} \\
R_2(\theta) &= \begin{bmatrix} \cos \theta & 0 & -\sin \theta \\ 0 & 1 & 0 \\ \sin \theta & 0 & \cos \theta \end{bmatrix} \\
R_3(\theta) &= \begin{bmatrix} \cos \theta & \sin \theta & 0 \\ -\sin \theta & \cos \theta & 0 \\ 0 & 0 & 1 \end{bmatrix}
\end{aligned} \tag{2.25}$$

2.4.3 Topocentric Reference Frame (ENU)

The remaining transformations in this chapter will only be defined in terms of their rotation matrices. It is often useful to express observations in a local reference frame. The East North Up (ENU) coordinate system is used throughout this work. This system has an origin at the observing station, with the first two basis vectors pointing towards the local East and North and the third pointing towards zenith. The transformation from ITRF to ENU is given by [4]:

$$\vec{r}_{enu} = F_2 F_1 R_2(\phi_{geoc}) R_3(\lambda) \vec{r}_{itr}. \tag{2.26}$$

In Eq 2.26, R_3 is a rotation about the third body axis, F_1 swaps the second and third unit vectors, and F_2 swaps the first and third unit vectors. The orientation of the ENU reference frame at the Purdue Optical Ground Station is depicted in Figure 2.5.

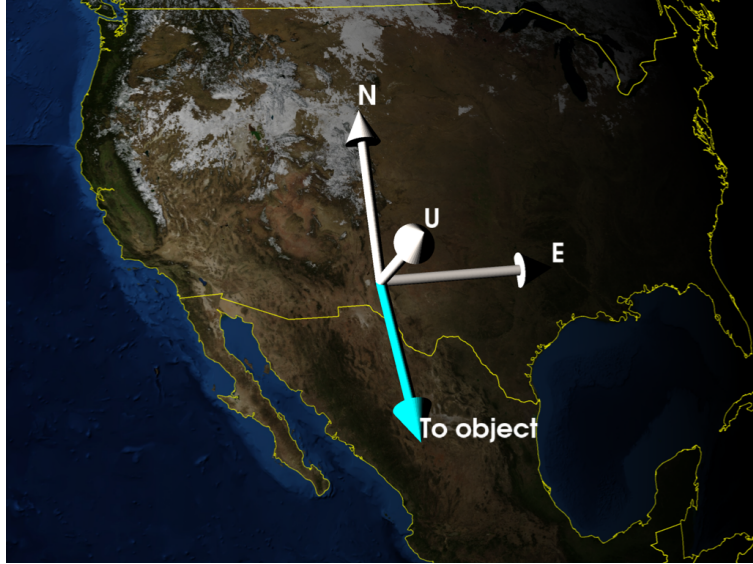


Figure 2.5. ENU reference frame orientation at Purdue Optical Ground Station

2.4.4 International Celestial Reference Frame (ICRF/J2000)

Transforming from ITRF to the a standardized inertial reference frame is an involved process due to the variety of nonlinear effects impacting the Earth's rotational motion. In total, this transformation must account for polar motion, the nutation and precession of the Earth's pole, and the mean sidereal time. These transformations are treated much more thoroughly in Vallado [3].

Accounting for polar motion — the motion of the Earth's pole that cannot be explained through nutation theory — transforms from ITRF to Greenwich True of Date (GTOD) via:

$$\vec{r}_{gtod} = R_1(y_p)R_2(x_p)\vec{r}_{itrif}, \quad (2.27)$$

where x_p and y_p are the angular components of the polar motion at the time of interest [4]. Accounting for the sidereal rotation of the Earth about its pole transforms from GTOD to the True Equator, Mean Equinox (TEME) reference frame via [4]:

$$\vec{r}_{teme} = R_3(-\theta_{GMST})\vec{r}_{gtod}. \quad (2.28)$$

Accounting for the difference between GMST and GAST at the date of interest transforms from TEME to the True of Date (TOD) reference frame via [3]:

$$\vec{r}_{tod} = R_3(-\Delta\Psi \cos \epsilon) \vec{r}_{teme}. \quad (2.29)$$

Accounting for the nutation of Earth's pole transforms from TOD to the Mean of Date (MOD) reference frame via:

$$\vec{r}_{mod} = R_1(-\bar{\epsilon})R_3(\Delta\Psi)R_1(\bar{\epsilon} + \Delta\epsilon)\vec{r}_{tod}, \quad (2.30)$$

where $\bar{\epsilon}$ is the mean inclination of the ecliptic at the time of interest, and ϵ is the true inclination of the ecliptic [3].

Accounting for the secular precession of Earth's pole transforms from MOD to ICRF via:

$$\vec{r}_{icrd} = R_3(\zeta)R_2(\theta)R_3(z)\vec{r}_{mod}, \quad (2.31)$$

through the 3-2-3 Euler angle sequence (z, θ, ζ) , which are each a function of the date of the transformation [4].

The specific realization of ICRF used in this work is referenced to the position of the equator and equinox at the J2000.0 epoch (January 1, 2000 12:00:00.000 TT), leading to the common name for this reference frame, "J2000" [3].

2.4.5 Right Ascension and Declination

Right ascension and declination, often shortened to RA/Dec, are useful angles from describing the angular position of an object on the celestial sphere from the perspective of an observer. Right ascension is defined as the angle of the observation projected onto the inertial $x - y$ plane, measured counterclockwise from inertial \hat{x} , represented by α . Declination is the angle from the $x - y$ plane to the observation with positive values above the $x - y$ plane (closer to inertial z) and negative values below. Declination is represented by δ . Given a unit vector direction $\hat{v} = [x_{ITRF}, y_{ITRF}, z_{ITRF}]^T$ in J2000, RA/Dec is computed via [4]:

$$\begin{bmatrix} \alpha \\ \delta \end{bmatrix} = \begin{bmatrix} \text{atan2}(y_{ITRF}, x_{ITRF}) \\ \text{atan2}(z_{ITRF}, \sqrt{x_{ITRF}^2 + y_{ITRF}^2}) \end{bmatrix}. \quad (2.32)$$

2.4.6 Azimuth and Elevation

Azimuth and elevation, often shortened to Az/El, are similar angular quantities to right ascension and declination [4]. Instead of being based on the inertial sphere, they are referenced to an arbitrary reference frame. For a telescope making observations of an object, the local topocentric ENU frame may be used. For a satellite star tracker, star azimuth and elevation might be reported in the satellite body frame. In either case, Eq 2.32 can be repurposed in terms of Az/El, where $\hat{v} = [x_{ENU}, y_{ENU}, z_{ENU}]^T$ is expressed in the frame of interest [4].

$$\begin{bmatrix} Az \\ El \end{bmatrix} = \begin{bmatrix} \text{atan2}(y_{ENU}, x_{ENU}) \\ \text{atan2}(z_{ENU}, \sqrt{x_{ENU}^2 + y_{ENU}^2}) \end{bmatrix} \quad (2.33)$$

Note that Eq 2.33 references azimuth to the x -axis, proceeding in the counterclockwise direction. Often, this reference axis and direction may be changed depending on the reference frame being used. For example, ground station observations may be referenced to local North — the second axis of the ENU system — proceeding clockwise. This would require the substitution $Az' = \frac{\pi}{2} - Az$. Notice that this substitution leads to Az' leaking outside the domain of $[0, 2\pi]$. This is not an issue for later coordinate transformations, but may be undesirable for plots. Wrapping the result back to the standard azimuth range via $Az_{wrapped} = \text{mod}(Az, 2\pi)$ is a sufficient fix.

2.4.7 Coordinate Transformations Summary

With these transformations, any topocentric observation directions in RA/Dec or Az/El can be converted into a Cartesian representation and transformed into J2000. Simultaneously, any propagated space object orbits can be transformed similarly from an arbitrary

propagation frame such that all future computations requiring the observation geometry take place in the same reference frame.

2.5 Photometry

2.5.1 The Charge Coupled Device (CCD)

Many optical telescopes, including the Purdue Optical Ground Station, use a CCD to convert incident photons into a digital signal on a pixel grid [9]. CCDs accomplish this with a matrix of semiconductor pixel wells which collect electrons released by the photoelectric effect when photons are incident on that pixel [9]. The release of these photoelectrons is wavelength dependent and is captured by the quantum efficiency spectrum of a given CCD. Developing this background in photometry is useful for both light curve simulation as well as simulating the CCD camera measuring that light curve.

2.5.2 Diffraction

Rayleigh Criterion

Many objects of interest are far past low-Earth orbit, making optical observations diffraction limited. Diffraction is always occurring when observing an object at any distance through any optics, but it begins to dominate when the object's scale is equal or smaller than the Rayleigh criterion. The Rayleigh criterion states that light of wavelength λ will spread into a diffraction pattern with the first minimum of the distribution at an angular radius θ_R when passing through a circular aperture of diameter d such that:

$$\sin \theta_R = \frac{1.22\lambda}{d}. \quad (2.34)$$

For a 1-meter aperture optical telescope observing a 10-meter diameter object in GEO — giving an angular radius of $\approx 10^{-7}$ radians — Eq 2.34 predicts that the diffraction pattern will be 5 times wider than the object. As a result, GEO objects cannot be resolved from the ground, independent of atmospheric effects.

The Airy Disk

The far-field diffraction pattern produced by a point source is known as an Airy pattern [4]. The Airy disk is expressed in terms of an amplitude C at an angular distance θ from the center $C(\theta)$ as:

$$C_{\text{Airy}}(\theta) = C_0 \left(\frac{2J_1(k \cdot r_d \sin \theta)}{k \cdot r_d \sin \theta} \right). \quad (2.35)$$

In Eq 2.35, C_0 is the amplitude of the center of the Airy disk, r_d is the radius of the aperture, $k = \frac{2\pi}{\lambda}$ is the wavenumber, and J_1 is the first order Bessel function of the first kind. The central magnitude C_0 is expressed:

$$C_0 = \frac{S_{\text{obj}}^2 A_{\text{aperture}}^2}{2f^4}. \quad (2.36)$$

In Eq 2.36, S_{obj} is the total mean irradiance incident on the CCD due to the source, A_{aperture} is the aperture area, and f is the focal length of the optics [4]. The pattern produced by Eq 2.35 is depicted in Figure 2.6.

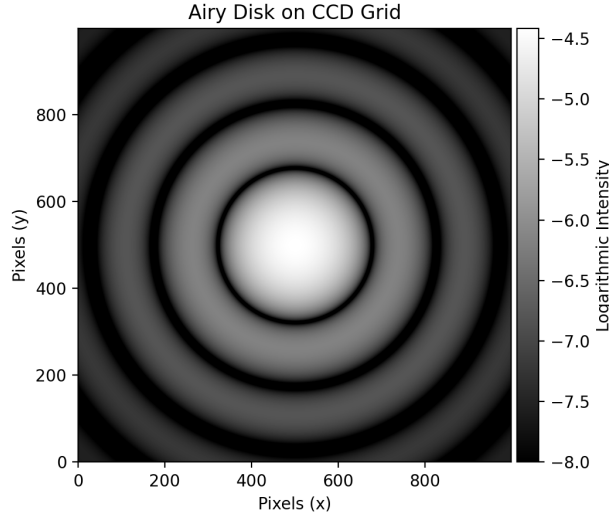


Figure 2.6. Airy disk diffraction pattern

The Rayleigh criterion expresses the angular size of the first zero of the Airy disk, after which the amplitude of the Airy disk drops off exponentially. It is often useful to approximate

the Airy disk with a 2D Gaussian. Given the total signal to be approximated, this Gaussian is fit with a single parameter — the full width at half maximum (FWHM). The FWHM expresses the diameter at which the signal drops to half the magnitude of its central maximum [4]. The FWHM of the Airy disk is expressed [4]:

$$FWHM_{\text{airy}} = \frac{1.028\lambda}{2r_d}. \quad (2.37)$$

The diffraction pattern is not the only effect that spreads the unresolved signal over the pixel grid. Atmospheric turbulence contributes to further spreading and speckling of the signal [4]. This effect — known as the *seeing* — is encapsulated in $FWHM_{\text{seeing}}$ and is generally between 1 and 3 arcseconds [4]. While the seeing and diffraction pattern are additive, it is sufficient to take the larger value for simulation purposes [4]. The standard deviation of the Gaussian approximation of the Airy disk is given by:

$$\sigma = \frac{FWHM}{2\sqrt{2 \ln 2}}. \quad (2.38)$$

The full Gaussian approximation at an angular distance θ from the source is given by:

$$C_{\text{Gauss}}(\theta) = \frac{0.838\bar{C}_{\text{all}}}{2\pi\sigma^2} \exp\left(-\frac{\theta^2}{2\sigma^2}\right) \quad (2.39)$$

In practice, computing the Airy disk or its Gaussian approximation on rectangular pixel grid amounts to integrating the amplitude function $C(\theta)$ over the pixel area:

$$C_{\text{pix}}(x, y) = \int_x^{x+\Delta x} \int_y^{y+\Delta y} C(\theta(x, y)) dy dx. \quad (2.40)$$

The area within the first maximum of the Airy disk is given by:

$$A_{\text{airy}} = \pi \left(\frac{648000/\pi}{s_{\text{pix}}} \sin^{-1} \left(\frac{1.22\lambda}{D} \right) \right)^2. \quad (2.41)$$

2.5.3 Signal-to-Noise Ratio (SNR)

Because the unresolved object signals are always superimposed on the background of the image, the SNR of a CCD is expressed with the signal included in the denominator noise term [4]:

$$SNR = \frac{S_{obj}}{\sqrt{S_{obj} + N}}. \quad (2.42)$$

Explicitly, the SNR can be expanded in terms of the signal means and variances [4]:

$$SNR = \frac{S_{obj}}{\sqrt{S_{obj+n_{pix}}(\lambda_{background} + \lambda_{dark} + \sigma_{read}^2 + \frac{g^2}{24})}}. \quad (2.43)$$

Figure 2.7 illustrates the effect of raising the background noise level while holding the object signal constant on the SNR.

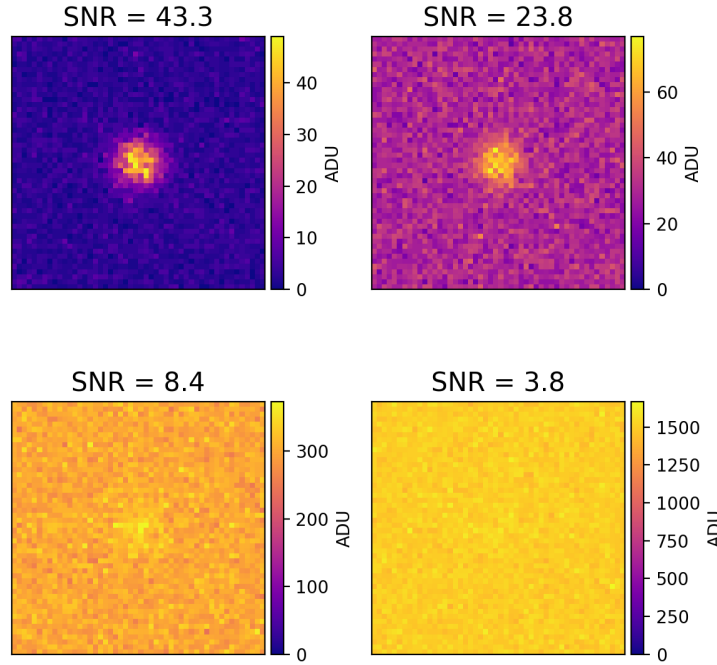


Figure 2.7. Signal-to-noise ratio reduction on a synthetic CCD pixel grid

The SNR is an important constraint when determining whether an object signal is visible above the background. If the SNR is too low, it becomes difficult or impossible to notice and quantify the object signal. Simulations in this work are all performed with a reasonable SNR limit of 3.

2.5.4 Brightness Units

In the context of photometry, "brightness" is a catch-all term for a variety of units. Let's explore the relationships between these units to make later conversions more clear. Brightness conversions are needed for both light curves and the environmental data sources that drive the CCD performance model described in Section 2.6.

Irradiance

Irradiance is the standard SI linear unit used to describe the total amount of energy incident on a surface from a given source. An irradiance of $1 \left[\frac{W}{m^2} \right]$ implies that a $10 [m^2]$ area would experience $10 [W]$ of incident power. The mean irradiance of the Sun — termed the solar constant — is derived from the mean luminosity of the Sun $L_s = 3.828 \cdot 10^{26} [W]$ and a distance of 1 Astronomical Unit $1 [AU] = 149597870.7 [km]$ [4]. The mean solar constant is then computed via

$$I_0 = \frac{L_s}{4\pi(AU)^2} \approx 1361.0 \left[\frac{W}{m^2} \right]. \quad (2.44)$$

In reality, the exoatmospheric irradiance at Earth varies [4]. Figure 2.8 displays the small variations in the solar irradiance due to the solar cycle and the much larger variations due to Earth's eccentric orbit.

Apparent Magnitude

Apparent magnitude — also known as visual or relative magnitude — is a reverse logarithmic scale that originates in astronomy [4]. Stellar sources span many orders of magnitude of brightness, making a logarithmic scale a helpful middle ground for comparison. Note that

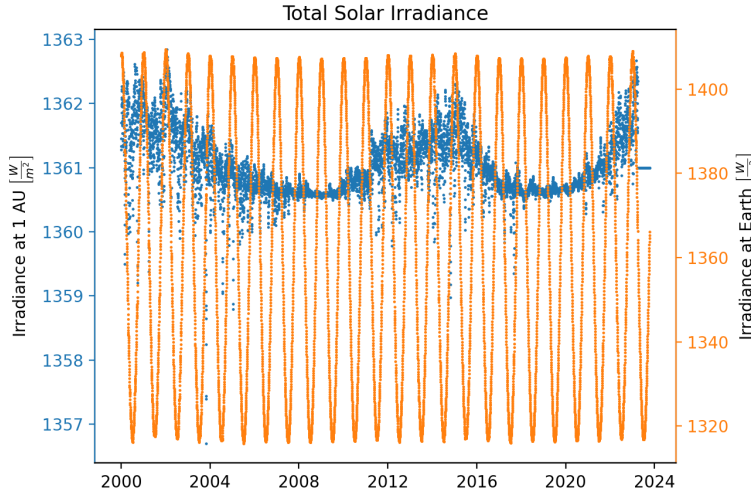


Figure 2.8. Total solar irradiance variations at Earth and 1 AU. The solar cycle is apparent when distance is held constant at 1 AU, yielding small variations in the peak intensity at Earth.

apparent magnitude always expresses brightness at the observer's location; absolute magnitude is a different quantity that normalizes brightness from a distance of 10 parsecs [4]. Apparent magnitude m is computed from irradiance via:

$$m = -2.5 \log_{10} \left(\frac{I}{I_z} \right). \quad (2.45)$$

In Eq 2.45, I is the irradiance of the source of interest and I_z is irradiance of the zero-point source. This makes sense; substituting $I = I_z$ returns $m = 0$. The star Vega is usually taken to be the zero-point with irradiance $I_z = 2.518021002 \cdot 10^{-8} \left[\frac{W}{m^2} \right]$ [4].

Eq 2.45 is rearranged to compute irradiance from a given apparent magnitude, yielding:

$$I = I_z \cdot 10^{-\frac{m}{2.5}}. \quad (2.46)$$

Normalized Irradiance

The light curve simulation methods presented in this work use normalized irradiance, the reflected irradiance of a object received at a distance of 1 meter illuminated by a distant source with an irradiance of 1 [W/m^2] at the object. This is a non-standard quantity in the literature, but proves useful for the same reasons absolute magnitude is used by astronomers. Adjusting sources to be at a standard distance enables the simulation and inversion of light curves in a non-dimensional environment. This simplifies simulation and makes the shape inversion optimizations more robust. To make the conversion explicit, irradiance observed at a distance r in meters from an object is converted to normalized irradiance due to the Sun \hat{I} via:

$$\hat{I} = \frac{r^2}{I_0} I. \quad (2.47)$$

S_{10} Surface Brightness

While apparent magnitude and irradiance are effective for quantifying the flux of point sources, other units exist to describe diffuse or extended sources where brightness is spread over an area. S_{10} is a unit of surface brightness representing the number of 10th magnitude stars per square degree that would produce the same flux as a given diffuse source. Surface brightness in S_{10} over a given solid angle Ω [sr] can be converted to total irradiance I [$\frac{W}{m^2}$] via:

$$\frac{I \left[\frac{W}{m^2} \right]}{S_{10}} = 10^{-10/2.5} \left(\Omega \frac{180^2}{\pi^2} \right) \int_{10^{-8}}^{10^{-6}} \text{STRINT}(\lambda) d\lambda = 8.26617 \Omega \cdot 10^{-9}. \quad (2.48)$$

In 2.48, $\text{STRINT}(\lambda) \left[\frac{W}{m^2 \cdot m} \right]$ is the representative spectrum of a 0th magnitude star, $\text{QE}(\lambda)$ is the quantum efficiency spectrum of the observing sensor, $\text{ATM}(\lambda)$ is the atmospheric transmission spectrum, $\lambda [m]$ is wavelength, $h \left[\frac{m^2 \cdot kg}{s} \right]$ is Plank's constant, and $c \left[\frac{m}{s^2} \right]$ is the speed of light in vacuum. Quantum efficiency has units of photoelectrons which conveys the fraction of incident photons which are (proportionally) converted to photoelectrons in the CCD sensor. Atmospheric transmission is a unitless quantity conveying the fraction of

light that is not absorbed by the atmosphere. Example spectra for $\text{ATM}(\lambda)$ and $\text{QE}(\lambda)$ are displayed in Figure 2.11, with underlying data provided in Appendices 5.2 and ??.

Magnitude per Square Arcsecond

A second surface brightness unit is $\left[\frac{\text{mag}}{\text{arcsec}^2}\right]$, also known as MPSAS (magnitude per square arcsecond). This quantity can be thought of as a generalized S_{10} , where instead of quantifying the number of stars of a certain magnitude in a solid angle, the equivalent magnitude of a single point source is measured. A surface brightness B_{10} in S_{10} can be converted into surface brightness B_{mag} in $\left[\frac{\text{mag}}{\text{arcsec}^2}\right]$ via:

$$B_{\text{mag}} = -2.5 \log_{10} \left(\frac{B_{10} \cdot 10^{-4}}{12960000} \right). \quad (2.49)$$

In Eq 2.49 S_{10} is first converted to the total irradiance per square degree, convert square degrees to square arcseconds, and transform the result back into apparent magnitude. MPSAS is converted to irradiance per steradian using 2.46:

$$I = \left(\frac{180}{3600\pi} \right)^2 I_0 \cdot 10^{-\frac{\text{MPSAS}}{2.5}}. \quad (2.50)$$

Candela

Some light pollution datasets are given in units that include candela. Candela is the SI base unit of luminous intensity defined by the International Committee for Weights and Measures as "Fixing the numerical value of the luminous efficacy of monochromatic radiation of frequency $540 \cdot 10^{12}$ Hz to be equal to exactly 683" [47]. This means that an isotropic green light source with frequency $540 \cdot 10^{12}$ Hz ($\lambda = 555$ nm) has a luminous efficacy of $K_{cd} = 683$ [lm/W] where lm stands for lumens. Luminous efficacy itself determines how well a source produces visible light. For a given wavelength, candela B_{cd} is converted to watts per steradian B_{wsr} via [47]:

$$B_{wsr}(\lambda) = \frac{B_{cd}}{K_{cd}(\lambda)}. \quad (2.51)$$

The luminous efficiency function $K_{cd}(\lambda)$ models the human eye's response to the visible spectrum [48]. Different fits of this function exist; the function proposed Sharpe et al. is adopted, displayed in Figure 2.9 [48].

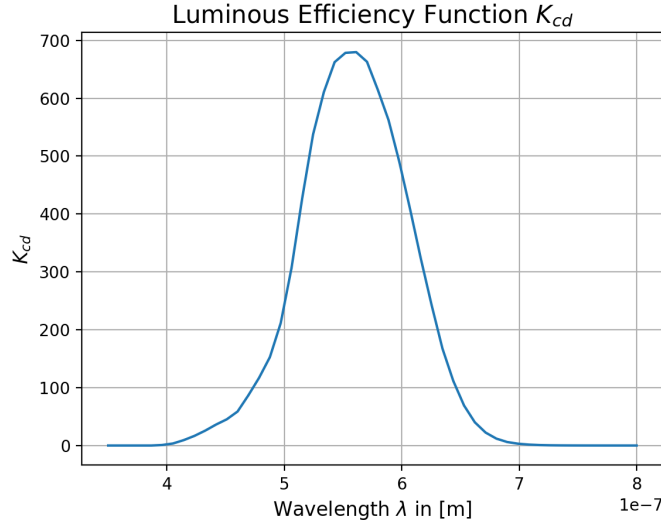


Figure 2.9. Luminous efficiency function from [48]

Candela per unit area can be converted into MPSAS by combining Eq 2.51 with 2.45, yielding a formulation which is still a function of the source's wavelength:

$$MPSAS(\lambda) = -2.5 \log_{10} \left(\frac{B_{cd}}{\left(\frac{180}{3600\pi} \right)^2 K_{cd}(\lambda) I_0} \right). \quad (2.52)$$

Photoelectron Counts

Accurately simulating measured light curves requires an accurate simulation of the CCD camera taking the image. The first step towards that is understanding how irradiance at the telescope aperture is converted into pixel values in the final image. Raw images taken by a CCD-equipped telescope have pixel values measured in photoelectron counts, otherwise known as Analog-to-Digital Units (ADU) [9]. The count in a single pixel obtained is directly proportional (via the CCD's gain) to the number of photons incident on that pixel during the integration time. Higher order effects in the silicon of the CCD makes this description

incomplete, but for non-resolved imaging applications concerned about, effects smaller than the sensor readout noise and dark current can be safely neglected [4]. Irradiance can be converted to ADU via the conversion factor $SINT$ through [9]:

$$SINT = A_{aperture} \int_{10^{-8}}^{10^{-6}} \left(\frac{\text{SUN}(\lambda)}{I_{sun}} \right) \cdot \text{QE}(\lambda) \cdot \text{ATM}(\lambda) \cdot \left(\frac{\lambda}{hc} \right) d\lambda. \quad (2.53)$$

In Eq 2.53, $\text{SUN}(\lambda)$ is the spectrum of solar irradiance in $\left[\frac{W}{m^2 \cdot m} \right]$, I_{sun} is the irradiance of the Sun (generally taken to be the solar constant 1361 $\left[\frac{W}{m^2} \right]$). Read literally, the integral term as units $\left[\frac{1}{W \cdot s} \right]$, giving the number of counts per incident Watt of solar radiation and second of integration time. The aperture diameter factor outside the imintegral accounts for the area of light incident on the CCD, giving SINT units of $\left[\frac{m^2}{W \cdot s} \right]$. The spectra in Eq 2.53 are plotted in Figure 2.11 with data in Appendix 5.2. Multiplying by irradiance in $\left[\frac{W}{m^2} \right]$ and an integration time Δt in seconds will yield the mean photoelectron signal \bar{C}_{all} in ADU via:

$$\bar{C}_{all} = \text{SINT} \cdot I \cdot \Delta t. \quad (2.54)$$

For completeness, irradiance can be recovered from a signal in ADU and the integration time:

$$I = \frac{S}{\text{SINT} \cdot \Delta t}. \quad (2.55)$$

2.5.5 The Light Curve

The light curve expresses the observed brightness of an object over time. In literature, that brightness is commonly expressed in terms of irradiance, apparent magnitude, or photoelectron counts. This work also considers the normalized irradiance for some simulation and inversion tasks. Converting between these representations is accomplished with Eqs 2.55 and 2.45.

Figure 2.10 details this equivalence with the same light curve expressed in these four unit systems. This figure also displays an important characteristic of real measured light curves: they are always contaminated with noise. As a result, the "true mean" signal in Figure

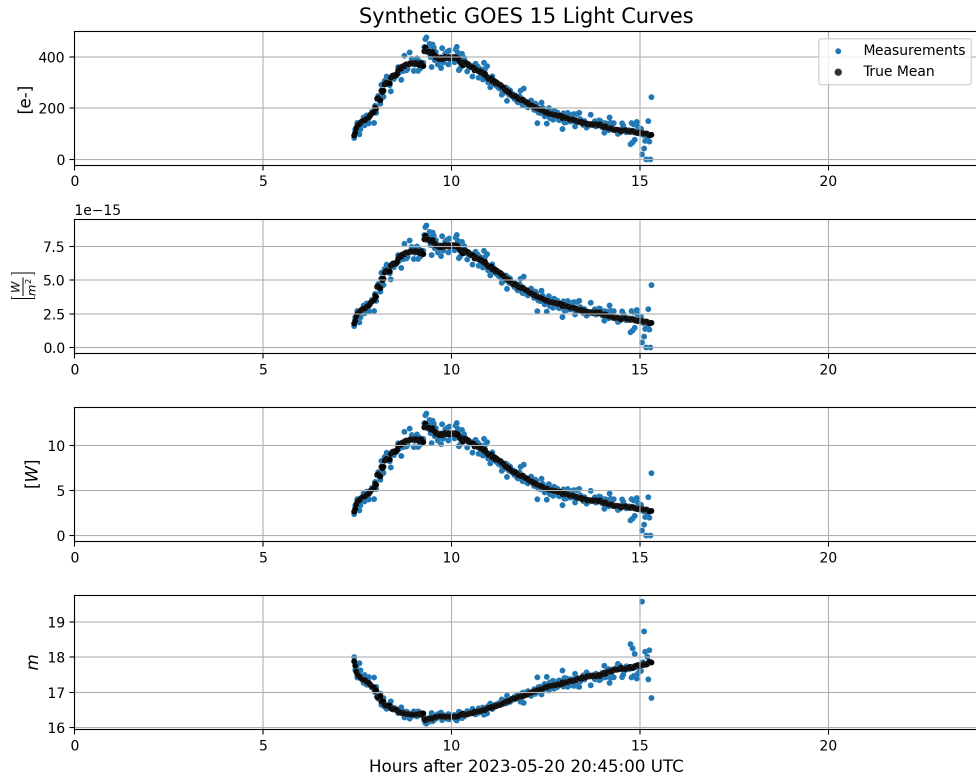


Figure 2.10. Synthetic light curves in counts, irradiance, normalized irradiance, and apparent magnitude

2.10 cannot be obtained through the raw measurements, and is merely computed here as a stepping stone to the measured digital signal in the CCD. The sources of this noise are described in detail in Section 2.6.

2.6 CCD Performance Model

Whenever an optical telescope is observing an unresolved space object, the object's signal is necessarily superimposed on whatever signals exist in the background as the unresolved signal spreads much further than the object's actual geometric bounds. In this context, background does not only refer to sources physically further than the object — as light can easily enter optical path through atmospheric scattering — but all sources that impact the image apart from the object signal. Some of these sources even originate within the

Source	Magnitude [e ⁻ /pix]
Twilight	$10^1 - 10^7$
Scattered moonlight	$0 - 10^5$
Airglow	$10^3 - 10^4$
Zodiacal light	$10^2 - 10^4$
Light pollution	$10^2 - 10^3$
Integrated starlight	$10^1 - 10^2$

Table 2.2. Background signal importance

telescope optics and its sensor. To faithfully simulate a telescope observing an object, many position-based SDA tasks are able to ignore background effects while acquiring or tracking objects. For photometry-based SDA, the background is critical. The overall noise floor can be broken up into background signal sources and sensor effects.

2.6.1 Background Signal Sources

Background Source Importance

Some background signals are more impactful than others. For simulating realistic light curves, it is important to only model those background sources that have the possibility of being at or above the order of magnitude of the object signal, thereby seriously degrading the signal-to-noise ratio. As a baseline, the background terms modeled by Krag for the PROOF CCD performance model were implemented, namely scattered moonlight, airglow, zodiacal light, and integrated starlight [9]. In addition, twilight and light pollution models were implemented to increase the time and station location flexibility of the simulation. Each background term is modeled at medium fidelity — often using tabulated measurements or set of exponential distributions to govern the scattering physics. As a result, this background performance model does not capture local weather conditions or precisely simulate the scattering of each photon through the atmosphere, but still strives to faithfully models the physics of each background signal process. Table 2.2 ranks the approximate magnitudes in photoelectrons per pixel one can expect from a telescope similar to the Purdue Optical Ground Station.

Astronomical Spectra

Four of the quantities needed for the background model vary with wavelength. These are the atmospheric transmission, the sensor quantum efficiency, the irradiance of a 0th magnitude star, and the solar spectrum. Each spectrum is displayed in Figure 2.11.

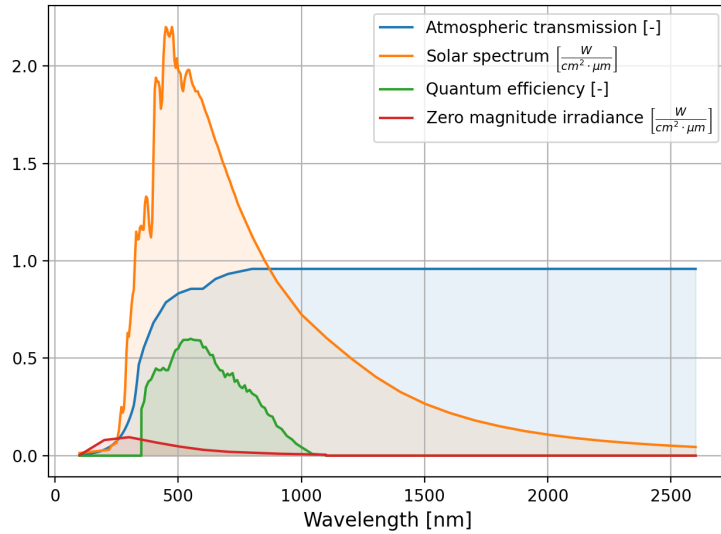


Figure 2.11. Astronomical Spectra, atmospheric transmission and zero magnitude stellar spectrum from [9]

In practice, the quantum efficiency curve varies by sensor and the thermal conditions of the observation. The curve adopted in this work is that used by Krag; modern sensors will often perform better.

Airglow

Certain chemical reactions from 80-110 km altitude in the upper atmosphere release visible light [9]. This effect is known as airglow. Since these reactions are assumed to be isotropic — equally intense when integrated along any vertical line extending upwards from the surface. The airglow signal AINT is modeled in a similar fashion to integrated starlight. Given the airglow spectra $GLINT(\lambda)$ $\left[\frac{W}{m^2 \cdot sr}\right]$, the airglow signal is computed via [9]:

$$\text{AINT} = A_{\text{aperture}} \int_{10^{-8}}^{10^{-6}} \text{GLINT}(\lambda) \cdot \text{QE}(\lambda) \cdot \text{ATM}(\lambda) \cdot \left(\frac{\lambda}{hc} \right) d\lambda. \quad (2.56)$$

The quantity AINT has units $\left[\frac{1}{\text{s}\cdot\text{sr}} \right]$, meaning that the mean airglow signal in ADU per pixel is simply given by:

$$\bar{S}_{\text{airglow}} = \text{AINT} \cdot \text{AM}(\theta_z) \cdot \Delta t \cdot \left(\frac{\pi s_{\text{pix}}}{648000} \right)^2. \quad (2.57)$$

In Eq 2.57, $\text{AM}(\theta_z)$ is the relative airmass function which accounts for the accumulation of air along the optical path at different zenith angles [4]. This airmass is termed *relative* as it relates the ratio of absolute airmass at a zenith angle to the absolute airmass at zenith. Often, this function is approximated by the Van-Rhijn factor $\text{AM}(\theta_z) = \sec \theta_z$ which remains accurate up to $\theta_z \approx 70^\circ$ before diverging to infinity. Instead, a function proposed by Pickering is used [49].

$$\text{AM}(\theta_z) = \frac{1}{\sin \left((90 - \theta_z) + \frac{244}{165 + 47 * (90 - \theta_z)^{1.1}} \right)} \quad (2.58)$$

Using Eq 2.58 instead of the Van-Rhijn factor enables the computation of background signals near the horizon without the singularity of $\sec \theta$. Figure 2.12 displays this comparison in action.

Light Pollution

Another source of background noise light pollution. On a cloudless night with low levels of atmospheric aerosols, the zenith surface brightness is approximately $22 \left[\frac{\text{mag}}{\text{arcsec}^2} \right]$ (MPSAS) [9]. As light pollution increases, this zenith brightness may dip down to $14 - 15 \left[\frac{\text{mag}}{\text{arcsec}^2} \right]$. To get accurate localized zenith brightness values, the 2015 World Atlas of Sky Brightness dataset is used [50]. The data is reported in $\left[\frac{\text{mcd}}{\text{cm}^2} \right]$ on a 30-arcsecond grid, requiring conversion to a more useful unit. A subset of the global dataset is displayed in 2.14. This conversion is listed in Eq 2.52, using a monochromatic $\lambda = 474$ nm to fit the conversions of Falchi et al. [51].

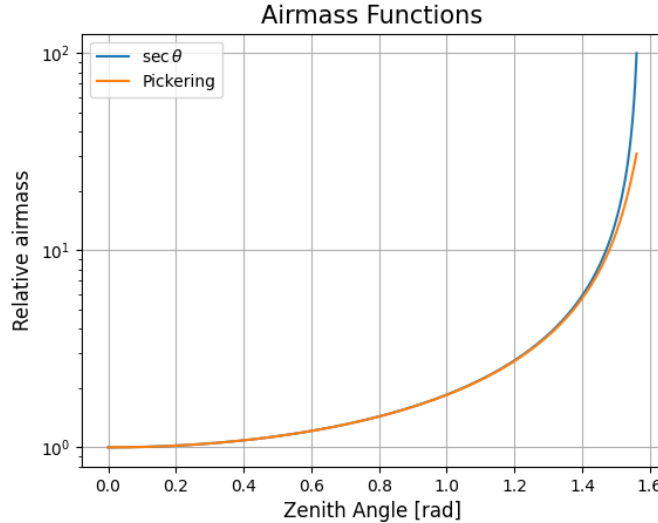


Figure 2.12. Airmass function comparison. The Van-Rhijn factor diverges to $+\infty$ while Pickering’s function reaches the correct maximum of $\text{AM}(\theta_z) \approx 40$.

The mean light pollution CCD signal in ADU per pixel is formulated similarly to airglow. The station’s zenith surface brightness $B_{poll,z}$ in MPSAS, linearly interpolated from the World Atlas dataset, is converted to irradiance per steradian via 2.50 and to ADU per pixel via:

$$\bar{S}_{pollution} = B_{poll,z} \cdot SINT \cdot \text{AM}(\theta_z) \cdot \Delta t \cdot \left(\frac{\pi s_{pix}}{648000} \right)^2. \quad (2.59)$$

Note that Krag does not implement a specific light pollution model, but instead takes the dark sky site zenith brightness of 22 MPSAS as input to an atmospherically scattered light model [9]. The formulation of the light pollution model in Eq 2.59 is simply an adaptation of Krag’s model with a variable zenith brightness driven by a light pollution dataset.

Twilight

Even after the Sun sets, scattered sunlight in the upper atmosphere creates a signal on the CCD. The twilight model implemented for this work is due to Patat et al. and was developed for the European Southern Observatory at Paranal in Chile [52]. This model implements the zenith brightness as a function of the solar zenith angle γ — the angle from zenith to

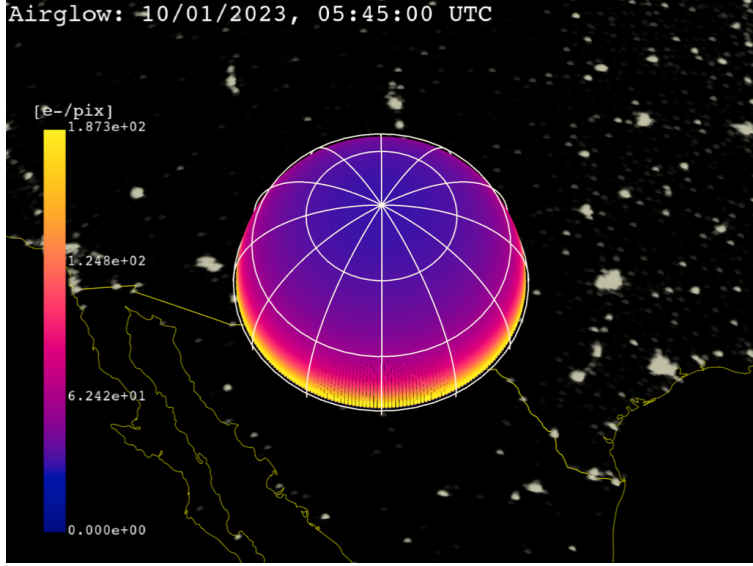


Figure 2.13. Mean airglow signal on the local observer hemisphere. The observer is in New Mexico, USA at 32.900° N , -105.533° W

the Sun’s apparent centroid. The model of Patat et al. fits a second-degree polynomial in γ to approximately 2000 observations in varying atmospheric conditions, yielding separate curves for each of the UBVRI passbands. For example, for the V band, the twilight zenith brightness in MPSAS is given by [52]:

$$B_{twi,z} = 11.84 + 1.518(\gamma - 95^\circ) - 0.057(\gamma - 95^\circ)^2. \quad (2.60)$$

Eq 2.60 is valid from $95^\circ \leq \gamma \leq 105^\circ$. While $\gamma \leq 95^\circ$, the zenith brightness is taken to be constant and equal to the brightness at $\gamma = 95^\circ$. This is not accurate, as it predicts daylight to be the brightness of twilight, but is sufficiently bright to correctly forbid daytime observations by lowering the SNR drastically. After $\gamma = 105^\circ$ the zenith surface brightness is set to $B_{twi,z} = 22$ MPSAS to match the optimal observation condition of the light pollution model [9]. Zenith twilight brightness is plotted as a function of γ in Figure 2.16.

Computing the mean CCD signal in ADU per pixel due to the twilight brightness proceeds identically to the light pollution formulation.

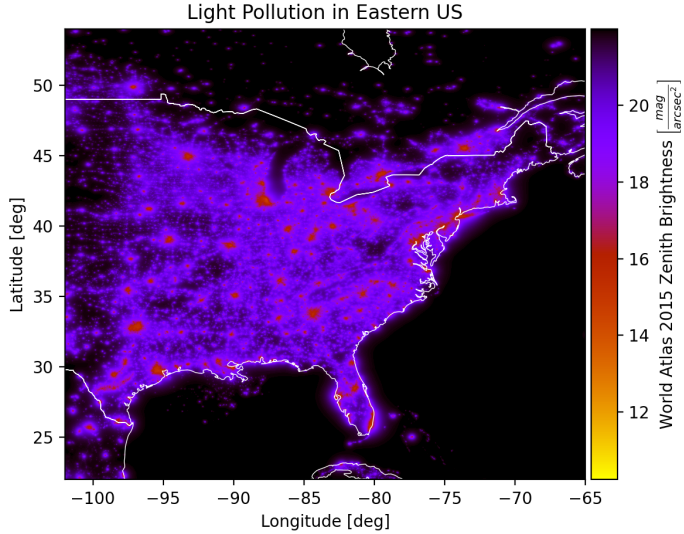


Figure 2.14. Zenith light pollution in the eastern USA, data from [50]

$$\bar{S}_{twilight} = B_{twi,z} \cdot SINT \cdot AM(\theta_z) \cdot \Delta t \cdot \left(\frac{\pi s_{pix}}{648000} \right)^2 \quad (2.61)$$

Integrated Starlight

Stars are almost always present in optical images of space objects. The brightest stars streaking across the field of view in Figure 2.18 have high SNRs and stand out clearly against the dark background. This raises a question: if the telescope observes a full $1^\circ \times 1^\circ$ area of the sky, where are the rest of the stars? The Milky Way alone contains approximately $1 \cdot 10^{11}$ stars. The answer is clear: many more stars are present in the image, most of them falling into the background. This residual faint starlight is called "integrated" starlight.

Krag [9] modeled this signal by building a $1^\circ \times 1^\circ$ grid of surface brightness values for the full inertial sphere, parameterized by RA/Dec. Krag used the Guide Star catalog, which contains 15 million stars down to apparent magnitude 16. Exponential extrapolation was used to predict star counts in each bin for higher magnitudes [9]. Twenty years later, larger star catalogs exist that are nearly complete to much higher apparent magnitudes.

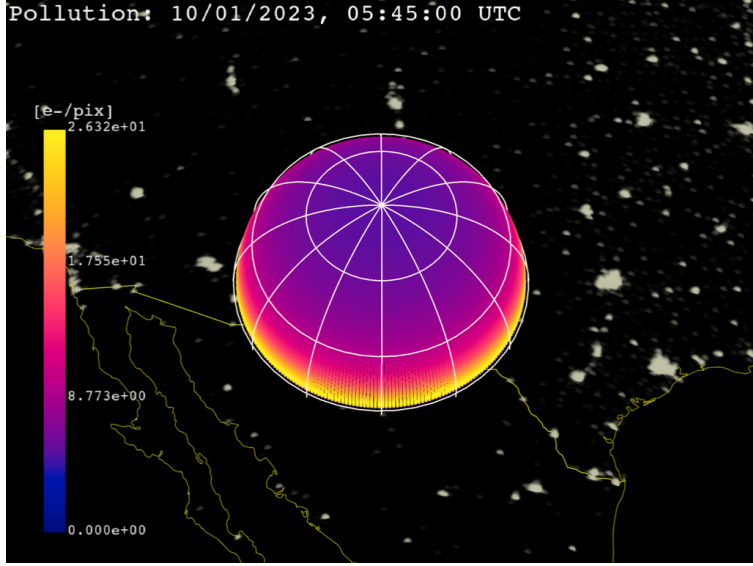


Figure 2.15. Mean light pollution signal on the local observer hemisphere. The observer is in New Mexico, USA at 32.900° N, -105.533° W

The integrated starlight catalog used in this work was built from the GAIA catalog with approximately 1.5 billion stars down to magnitude 21-22 [53]. The same $1^{\circ} \times 1^{\circ}$ grid was computed using GAIA [54], resulting in Figure 2.19 which shows the computed brightness map in units of S_{10} .

With this map of exoatmospheric mean brightness of the night sky due to integrated starlight, the corresponding signal mean in the telescope CCD is computed, adopting Krag's formulation [9].

$$BINT = A_{aperture} \int_{10^{-8}}^{10^{-6}} \text{STRINT}(\lambda) \cdot \text{QE}(\lambda) \cdot \text{ATM}(\lambda) \cdot \left(\frac{\lambda}{hc} \right) d\lambda \quad (2.62)$$

In Eq 2.62, D is the telescope aperture diameter in meters, h is Plank's constant in $\left[\frac{m^2 kg}{s} \right]$, and c is the speed of light in vacuum in $\left[\frac{m}{s} \right]$. The resulting quantity BINT has units of $\left[\frac{1}{s} \right]$, representing the mean total photons passing through the telescope aperture due to integrated starlight.

$$\bar{S}_{star} = 10^{-4} \cdot BINT \cdot \left(\frac{s_{pix}}{3600} \right)^2 \cdot \Delta t \cdot b_{is} \quad (2.63)$$

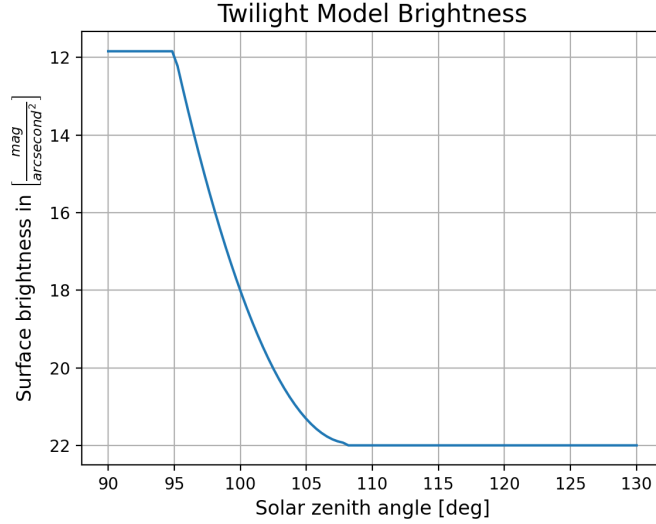


Figure 2.16. Twilight model surface brightness at zenith as a function of solar zenith angle

In Eq 2.63, b_{is} is the integrated starlight brightness in $[S_{10}]$ computed by linearly interpolating the dataset in Figure 2.19, s_{pix} is the telescope pixel scale in $\left[\frac{\text{arcsecond}}{\text{pix}}\right]$, and Δt is the integration time in seconds. Note the addition of the 10^{-4} factor to reconcile catalog surface brightness in terms of 10th magnitude stars, and the 0th magnitude source in BINT. This yields \bar{S}_{star} with units $\left[\frac{\text{e}^-}{\text{pix}^2}\right]$; photoelectron counts (ADU) per pixel. Figure 2.20 shows the background signal mean due to integrated starlight.

Scattered Moonlight

Moonlight scattering through the atmosphere significant increases background brightness [9]. This scattering effect can be decomposed into Rayleigh (isotropically distributed) and Mie (exponentially distributed) scattering modes. The Rayleigh scattered component is computed with Table 4 published by Daniels parameterized by the angle from the observation to zenith z_{obs} , the angle from the Moon to zenith z_{moon} , and the angle between the observation and the Moon on the horizon ΔAz [55]. Interpolating this table yields the intensity of the

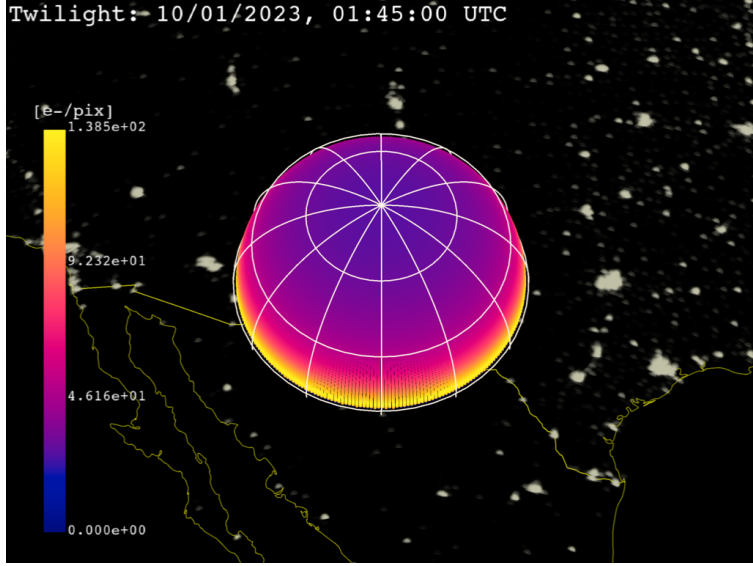


Figure 2.17. Mean twilight signal on the local observer hemisphere. The observer is in New Mexico, USA at 32.900° N , -105.533° W

Rayleigh scattering F_{rs} in $10^{-10} \text{ W}/(\text{cm}^2 \cdot \mu\text{m} \cdot \text{sr})$ [9]. The Mie scattered component is formulated [9]:

$$F_{ms}(\lambda) = a_1 \left[e^{-\left(\frac{\Psi}{\Psi_1}\right)} + a_2 e^{-\left(\frac{\pi-\Psi}{\Psi_2}\right)} \right] F_{rs}(\lambda). \quad (2.64)$$

Daniels recommends $a_1 \in [50, 100]$, $a_2 \in [0.01, 0.02]$, $\Psi_1 \in [10^\circ, 20^\circ]$, and $\Psi_2 \approx 50$ [55]. Prior to any station-specific fitting, the middle of these intervals are chosen, yielding $a_1 = 75$, $a_2 = 0.015$, $\Psi_1 = 15^\circ$, and $\Psi_2 = 50^\circ$. a_1 and a_2 are dimensionless, such that F_{ms} also has units of $10^{-10} \text{ W}/(\text{cm}^2 \cdot \mu\text{m} \cdot \text{sr})$. The total intensity of the scattered moonlight F_{mt} following Krag's formulation [9]:

$$F_{mt} = f(\theta) [F_{rs}(\lambda) + F_{ms}(\lambda)]. \quad (2.65)$$

in Eq 2.65, $f(\theta)$ is the lunar phase function which describes the fraction of the full Moon brightness reflected at an observer when the Sun-Moon-observer angle is θ . This function is linearly interpolated within Table 3 in [55]. Finally, Krag introduces a correction factor

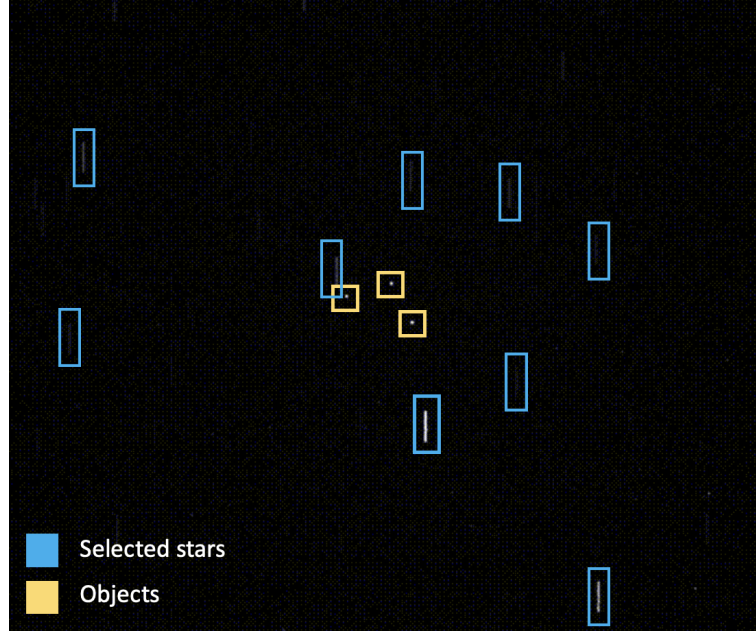


Figure 2.18. Raw image of three GEO objects with stars streaking through the background. As expected the star signals have a variety of signal-to-noise ratios. Taken by the Purdue Optical Ground station at 32.900° N, -105.533° W by Nathan Houtz.

f_{corr} to account for the difference between the Sun's irradiance spectrum and the spectrum of scattered moonlight, defined to be [9]:

$$f_{corr} = \frac{I_0}{SUN(550 \text{ [nm]})}. \quad (2.66)$$

With all these pieces, the mean scattered moonlight signal in ADU per pixel is:

$$\bar{S}_{moon} = F_{mt}(550 \text{ [nm]}) \cdot SINT \cdot \left(\frac{s_{pix}}{3600} \right)^2 \cdot \Delta t \cdot f_{corr}. \quad (2.67)$$

Zodiacal Light

Zodiacal light is an effect created by sunlight reflecting off of dust in the ecliptic plane [9]. Zodiacal light is strongest around the Sun — an exclusion zone for most optical telescopes — but also reaches a peak directly away from the Sun due to the opposition effect. This

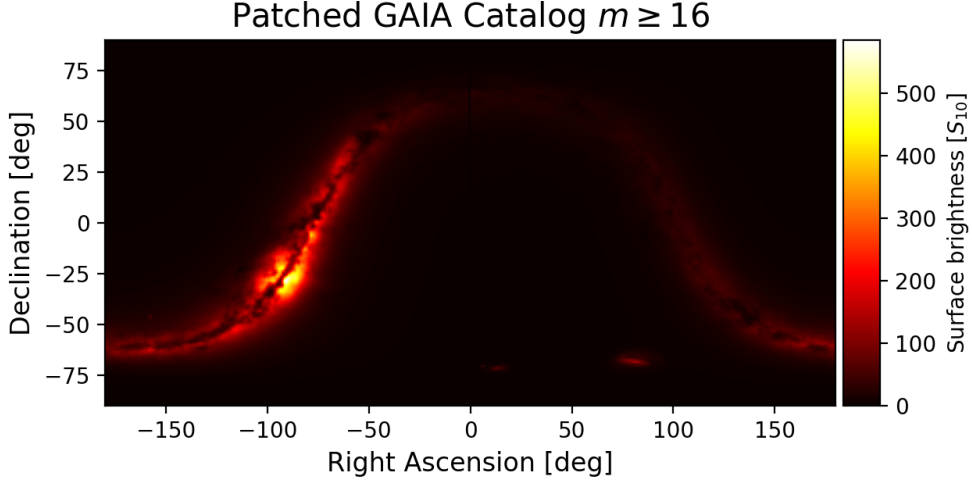


Figure 2.19. Integrated starlight brightness map

peak is known as the Gegenschein, meaning "opposing light". The zodiacal light brightness is linearly interpolated within Table 1 of [56] which is listed for convenience in Appendix 5.2.1. This reports the surface brightness of the zodiacal light in S_{10} , which is used without conversion to find the mean CCD signal in ADU per pixel via:

$$\bar{S}_{zod} = BINT \cdot \left(\frac{s_{pix}}{3600} \right)^2 \cdot \Delta t \cdot ZOD \cdot 10^{-4}. \quad (2.68)$$

As in the integrated starlight signal, the 10^{-4} factor reconciles the S_{10} surface brightness with the 0th magnitude source in BINT.

Background Sampling

The background signals are only defined in terms of their means, as each signal models the expected amount of radiation without accounting for the quantized nature of light [9].

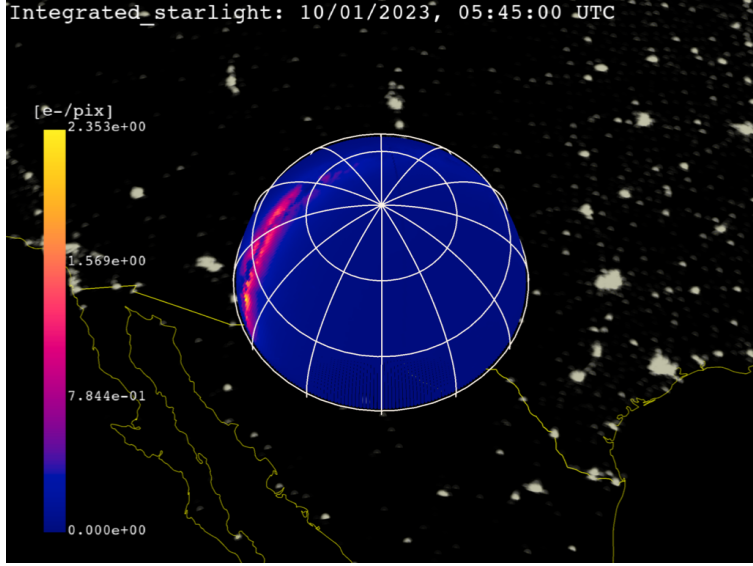


Figure 2.20. Integrated starlight signal on the local observer hemisphere. The observer is in New Mexico, USA at 32.900° N, -105.533° W

Since light is transmitted in individual photons, their incidence on a given pixel will follow a statistical distribution. Assuming that each photon does not interact with others, the incidence of a photon on a pixel is well-modeled as a Poisson process for each background term [4]. This distribution models the number of independent and identically distributed events that occur during a time period. For CCD astronomy, this translates to the event of a photon hitting the sensor. A Poisson distribution is defined on the positive integers by a single parameter λ which is both the mean and variance of the distribution. The probability density function (PDF) for the Poisson distribution takes the form [4]:

$$P_{\lambda}(x = k) = \frac{\lambda^k e^{-\lambda}}{k!}. \quad (2.69)$$

This distribution has a useful property that $P_{\lambda_1+\lambda_2}(x = k) = P_{\lambda_1}(x = k) + P_{\lambda_2}(x = k)$ so long as the distributions described by λ_1 and λ_2 are independent. The background sources modeled in this work are reasonably assumed to be independent as they each originate from distinct physical processes.

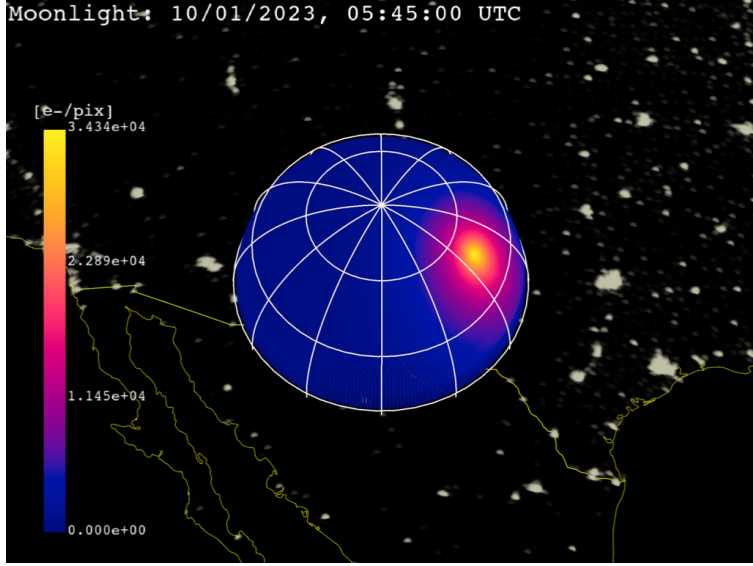


Figure 2.21. Mean scattered moonlight signal on the local observer hemisphere. The observer is in New Mexico, USA at 32.900° N, -105.533° W

$$\lambda_{background} = \bar{S}_{airglow} + \bar{S}_{pollution} + \bar{S}_{twilight} + \bar{S}_{star} + \bar{S}_{moon} + \bar{S}_{zod} \quad (2.70)$$

Drawing samples from the Poisson distribution defined by $\lambda_{background}$ computes the background of the CCD image.

2.6.2 Sensor Effects

Dark Noise

The dark noise, also called the dark current or dark count, captures the temperature-dependent accumulation of electrons in the CCD pixel wells [9]. This noise source is modeled as a Poisson process with parameter λ_{dark} [4] and is assumed to be independent from the other sensor effects. This source accumulates with the integration time, giving it units of counts per second [9].

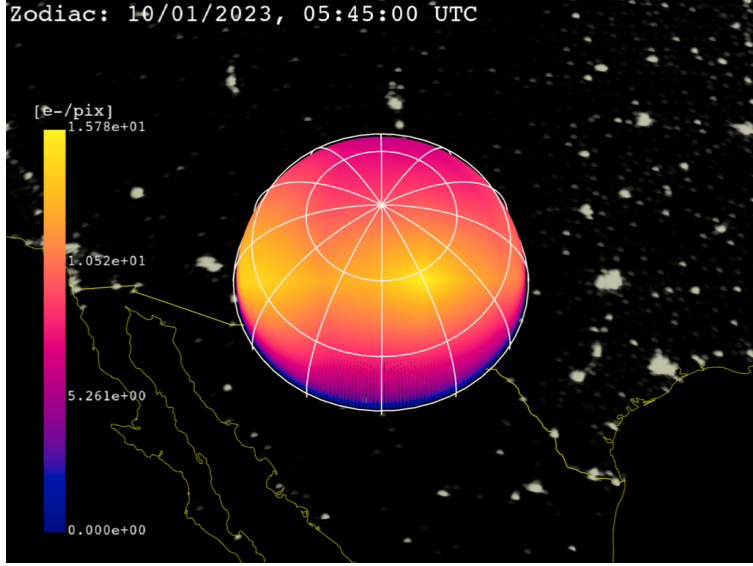


Figure 2.22. Mean zodiacal light signal on the local observer hemisphere. The observer is in New Mexico, USA at 32.900° N, -105.533° W

Readout Noise

When the CCD is read out, the charge contained in each pixel well must be digitized. This process introduces noise in the final signal due to electronic effects within the CCD circuitry and its surrounding environment [9]. The readout noise is modeled as a zero-mean Gaussian distribution with variance σ_{read}^2 and is also assumed to be independent from other sensor effects [4].

Truncation Noise

Truncation noise in a CCD stems from the fact that the charge in each pixel is digitized into an integer factor of the gain [4]. This is modeled using a uniform distribution on $[-g/2, g/2]$, yielding a variance $N_{trunc}^2 = \frac{g^2}{24}$ [4].

The particular noise variances for the Purdue Optical Ground Station are listed in ??.

3. Recommendations

4. Future Work

The next step with this work would be to extensively validate the CCD performance model against real observations taken by the Purdue Optical Ground Station. This would involve quantifying the sensor noise sources through zero second exposures and closed shutter exposures to isolate the effects of the dark noise and readout noise. Next, the background model would be fit to an array of observations at different times of the night, zenith angles, and lunar phases. Once both the background and sensor effects are well-calibrated, the overall CCD model can be tested against the observed signal counts and light curve SNR of known objects.

More work must also be done to perform light curve inversion on actively-controlled box-wing satellites. This would involve a simple adaptation of the EGI inversion method where some normal vectors are allowed to move in the body frame, enabling solar panels to track the Sun. Such a parametric approach could be used to check whether the light curve of an unknown object — in an unknown attitude profile — fits the expected light curve of a box-wing satellite with Sun tracking solar panels.

Finally, investigating shape inversion with multispectral measurements may open new avenues for simultaneously estimating attitude or material properties in addition to a convex shape. This might be accomplished operationally by switching filters between images, or by using a dedicated multispectral sensor. In either case, adding a second axis to the available data would enable far more robust characterization of space objects with fewer assumptions.

5. Appendices

5.1 Shadow Mapping

5.1.1 Shading

Algorithm 1 Pixel-wise shading algorithm with shadow mapping

$L \in \mathbb{S}^2$	▷ Unit vector from object origin towards Sun
$O \in \mathbb{S}^2$	▷ Unit vector from object origin towards observer
$N \in \mathbb{S}^2$	▷ Outward-pointing surface normal vector at pixel coordinates
$(C_d, C_s, n) \in \mathbb{S}^2$	▷ Reflection coefficients and exponent for the BRDF
Require: $C_d + C_s \leq 1$	▷ Enforce energy conservation
$MVP_{Sun} \in \mathbb{R}^{4 \times 4}$	▷ MVP matrix for the Sun camera
$(x, y) \in \mathbb{Z}^2$	▷ Integer pixel coordinates from the observer camera
$R_{pix,obs} \in \mathbb{R}^3$	▷ World coordinates of the pixel; provided by OpenGL
$[(x_{homo,Sun}, y_{homo,Sun}, \dots)] \leftarrow MVP_{Sun} [R_{pix,obs}, 1]^T$	
$x_{Sun} \leftarrow (1 + p_{x,homo}) \frac{w_{pix}}{2}$	▷ Homogeneous coordinates from the Sun camera
$y_{Sun} \leftarrow (1 + p_{y,homo}) \frac{a \cdot w_{pix}}{2}$	
$D_{Sun} \leftarrow d(x_{Sun}, y_{Sun})$	▷ Closest pixel depth to the Sun direction
$D_{obs} \leftarrow (L - O) \cdot L$	▷ Closest pixel depth in the Observer direction
if $D_{obs} > D_{Sun}$ then	
$\delta_{ss} = 1$	▷ Pixel is self-shadowed
else	
$\delta_{ss} = 0$	▷ Pixel may be illuminated
end if	
if $(N \cdot L) > 0$ and $(N \cdot O) > 0$ then	
$f_r(\mathbf{x}, L \rightarrow O) = 0$	▷ Pixel cannot be both observed and illuminated
else	
$f_r(\mathbf{x}, L \rightarrow O) = \text{Phong}(L, O, N, C_d, C_s, n)$	▷ The pixel is shaded with the BRDF
end if	
$\text{IM}(x, y) = f_r(\mathbf{x}, L \rightarrow O) (N \cdot L)$	▷ Image pixel value

5.2 Astronomical Spectra Data

Atmospheric Extinction

The atmospheric extinction coefficient is dimensionless.

```
{"lambda": [0.0, 3.2e-07, 3.400000000000003e-07, 3.6e-07, 3.79999999999996e-07, 4e-07, 4.5e-07, 5e-07, 5.5e-07, 6e-07, 6.5e-07, 7e-07, 8e-07, 0.001], "extinction": [5.0, 0.96, 0.54, 0.42, 0.34, 0.27, 0.17, 0.13, 0.11, 0.11, 0.07, 0.05, 0.03, 0.0]}

---


```

5.2.1 Background Source Data

Lunar Phase Factor

The lunar phase factor is a function of the phase angle in radians and is dimensionless.

```
{"phase_factor": [1.00, 0.809, 0.685, 0.483, 0.377, 0.288, 0.225, 0.172, 0.127, 0.089, 0.061, 0.041, 0.077, 0.017, 0.009, 0.004, 0.001, 0.0, 0.0], "phase_angle": [0, 0.17453293, 0.34906585, 0.52359878, 0.6981317 , 0.87266463, 1.04719755, 1.22173048, 1.3962634 , 1.57079633, 1.74532925, 1.91986218, 2.0943951 , 2.26892803, 2.44346095, 2.61799388, 2.7925268 , 2.96705973, 3.14159265]}
```

Scattered Moonlight

The scattered moonlight radiance in $\left[\frac{W}{sr \cdot m^2 \cdot m} \right]$ is a function of the difference in the line of sight and Moon azimuths `delta_az` in radians, the zenith angle of the moon `z_moon` in radians, and the zenith angle of the line of sight `z_obs` in radians.

```
{"z_obs": [0.0, 0.17453292519943295, 0.3490658503988659, 0.5235987755982988,  
0.6981317007977318, 0.8726646259971648, 1.0471975511965976, 1.2217304763960306,  
1.3962634015954636], "delta_az": [0.0, 0.7853981633974483, 1.5707963267948966,  
2.356194490192345, 3.141592653589793], "z_moon": [0.0, 0.5235987755982988,  
1.0471975511965976, 1.3089969389957472], "radiance": [[[22.0, 19.0, 13.0, 10.0],  
[22.0, 19.0, 13.0, 10.0], [22.0, 19.0, 13.0, 10.0], [22.0, 19.0, 13.0, 10.0], [22.0,  
19.0, 13.0, 10.0]], [[22.0, 21.0, 15.0, 11.0], [22.0, 20.0, 14.0, 11.0], [22.0,  
19.0, 13.0, 10.0], [22.0, 18.0, 12.0, 9.7], [22.0, 18.0, 12.0, 9.6]], [[22.0, 23.0,  
18.0, 13.0], [22.0, 22.0, 16.0, 12.0], [22.0, 19.0, 14.0, 10.0], [22.0, 17.0, 12.0,  
9.9], [22.0, 17.0, 12.0, 10.0]], [[22.0, 25.0, 21.0, 16.0], [22.0, 23.0, 18.0,  
14.0], [22.0, 20.0, 14.0, 11.0], [22.0, 17.0, 12.0, 11.0], [22.0, 16.0, 12.0,  
11.0]], [[23.0, 28.0, 25.0, 20.0], [23.0, 25.0, 21.0, 17.0], [23.0, 21.0, 16.0,  
12.0], [23.0, 17.0, 14.0, 13.0], [23.0, 16.0, 14.0, 14.0]], [[24.0, 31.0, 31.0,  
25.0], [24.0, 28.0, 26.0, 20.0], [24.0, 22.0, 18.0, 15.0], [24.0, 18.0, 17.0, 16.0],  
[24.0, 18.0, 18.0, 18.0]], [[27.0, 37.0, 39.0, 33.0], [27.0, 33.0, 32.0, 26.0],  
[27.0, 25.0, 22.0, 18.0], [27.0, 22.0, 22.0, 21.0], [27.0, 22.0, 25.0, 26.0]],  
[[34.0, 47.0, 54.0, 48.0], [34.0, 41.0, 43.0, 37.0], [34.0, 33.0, 29.0, 25.0],  
[34.0, 30.0, 33.0, 32.0], [34.0, 31.0, 40.0, 40.0]], [[55.0, 72.0, 89.0, 82.0],  
[55.0, 65.0, 71.0, 63.0], [55.0, 54.0, 50.0, 43.0], [55.0, 54.0, 61.0, 58.0], [58.0,  
58.0, 76.0, 75.0]]]}
```

Zodiacal Light

The zodiacal light surface brightness in S_{10} is a function of the latitude "ecliptic_lat" and longitude "ecliptic_lon" of the line of sight in the solar system ecliptic reference frame, both expressed in radians.

```
{"ecliptic_lat": [0.0, 0.17453292519943295, 0.3490658503988659, 0.5235987755982988, 0.6981317007977318, 0.8726646259971648, 1.0471975511965976, 1.2217304763960306, 1.3962634015954636], "ecliptic_lon": [3.141592653589793, 2.792526803190927, 2.443460952792061, 2.0943951023931953, 1.7453292519943295, 1.3962634015954636, 1.1344640137963142, 1.0471975511965976, 0.9599310885968813, 0.8726646259971648, 0.7853981633974483, 0.6981317007977318, 0.6108652381980153, 0.5235987755982988, 0.4363323129985824, 0.3490658503988659, 0.2617993877991494, 0.17453292519943295, 0.08726646259971647, 0.0], "brightness": [[[258.0, 211.0, 206.99999999999997, 239.0, 277.0, 365.0, 535.0, 630.0, 756.0, 939.0, 1190.0, 1490.0, 2010.0000000000002, 2940.0, 4660.0, 7690.000000000001, 15100.0, 36500.0, 176000.0, 16300000.0], [212.0, 194.0, 185.0, 217.0, 247.0000000000003, 312.0, 418.0, 455.0, 512.0, 603.0, 696.0, 825.0, 1150.0, 1550.0, 1820.0, 2140.0, 2760.0, 2720.0, 5630.0, 19900.0], [183.0, 174.0, 168.0, 196.0, 220.0000000000003, 258.0, 330.0, 339.0, 358.0, 403.0, 442.0, 512.0, 635.0, 800.0, 932.0, 1070.0, 1120.0, 1390.0, 1700.0, 2290.0], [159.0, 153.0, 152.0, 177.0, 196.0, 219.0, 258.0, 270.0, 282.0, 290.0, 304.0, 331.0, 363.0, 417.0, 491.0, 542.0, 592.0, 655.0, 724.0, 794.0], [141.0, 137.0, 137.0, 161.0, 175.0, 190.0, 204.0, 212.0, 229.0, 227.0, 233.0, 240.0, 224.0000000000003, 241.0, 246.0, 252.0, 265.0, 290.0, 315.0, 403.0], [127.0, 127.0, 128.0, 146.0, 156.0, 166.0, 165.0, 166.0, 183.0, 185.0, 189.0, 186.0, 171.0, 180.0, 183.0, 186.0, 190.0, 199.0, 209.0, 252.0], [117.0, 120.0, 120.0, 132.0, 139.0, 146.0, 137.0, 137.0, 147.0, 149.0, 150.0, 149.0, 137.0, 141.0, 144.0, 145.0, 145.0, 145.0, 146.0, 150.0], [110.0000000000001, 112.0000000000001, 112.0000000000001, 120.0, 123.0, 127.0, 118.0, 120.0, 124.0, 124.0, 124.0, 126.0, 118.0, 120.0, 121.0, 121.0, 121.0, 121.0, 121.0], [103.0, 105.0, 105.0, 108.0, 111.0000000000001, 111.0000000000001, 106.0, 107.0, 107.0, 108.0, 107.0, 111.0000000000001, 107.0, 106.0, 108.0, 108.0, 108.0, 108.0, 108.0]]}]}
```

5.2.2 Telescope Parameters

Purdue Optical Ground Station

5.2.3 File Formats

Wavefront OBJ Example

Parameter	Value
FWHM	1.5
Sensor dimensions	$0.03690 \times 0.03690 [m]$
<i>f</i> number	7.2
Aperture diameter D	0.35560 [m]
Secondary diameter	0.1724660 [m]
Sensor pixels	4096×4096
Pixel size	$9.009 \cdot 10^{-6} [m/\text{pix}]$
Pixel scale s_{pix}	0.72545 [arcsec]
Field of view	$0.824425^\circ \times 0.824425^\circ$
Integration time Δt	10 [s]
Integration dark noise λ_{dark}	3 [$\text{e}^-/\text{pix}/\text{s}$]
Read noise variance σ_{read}^2	9 [e^-]
CCD gain g	1

Table 5.1. Purdue Optical Ground Station telescope parameters

```
# Blender v2.92.0 OBJ File: ''
# www.blender.org
mtllib cube.mtl
o Cube_Cube.003
v 1.000000 1.000000 -1.000000
v 1.000000 1.000000 1.000000
v 1.000000 -1.000000 -1.000000
v 1.000000 -1.000000 1.000000
v -1.000000 1.000000 -1.000000
v -1.000000 1.000000 1.000000
v -1.000000 -1.000000 -1.000000
v -1.000000 -1.000000 1.000000
vt 0.625000 0.000000
vt 0.375000 0.250000
vt 0.375000 0.000000
vt 0.625000 0.250000
vt 0.375000 0.500000
vt 0.625000 0.500000
vt 0.375000 0.750000
vt 0.625000 0.750000
vt 0.375000 1.000000
vt 0.125000 0.750000
vt 0.125000 0.500000
vt 0.875000 0.500000
vt 0.625000 1.000000
vt 0.875000 0.750000
vn 1.0000 0.0000 0.0000
vn 0.0000 -1.0000 0.0000
vn -1.0000 0.0000 0.0000
vn 0.0000 1.0000 0.0000
vn 0.0000 0.0000 -1.0000
vn 0.0000 0.0000 1.0000
usemtl None
s off
f 2/1/1 3/2/1 1/3/1
f 4/4/2 7/5/2 3/2/2
f 8/6/3 5/7/3 7/5/3
f 6/8/4 1/9/4 5/7/4
f 7/5/5 1/10/5 3/11/5
f 4/12/6 6/8/6 8/6/6
f 2/1/1 4/4/1 3/2/1
f 4/4/2 8/6/2 7/5/2
f 8/6/3 6/8/3 5/7/3
f 6/8/4 2/13/4 1/9/4
f 7/5/5 5/7/5 1/10/5
f 4/12/6 2/14/6 6/8/6
```

REFERENCES

- [1] ESA Space Debris Office, “Esa’s annual space environment report,” European Space Agency, Tech. Rep., Apr. 2022.
- [2] N. G. S. F. Center, *Vanguard 1*, <https://nssdc.gsfc.nasa.gov/nmc/spacecraft/display.action?id=1958-002B>, Accessed: 2023-09-04.
- [3] D. Vallado, *Fundamentals of Astrodynamics and Applications*, 4th ed. J. Wertz, Ed. Microcosm Press, Mar. 2013.
- [4] C. Frueh, *Space traffic management*, Lecture Notes, 2019.
- [5] S. Fan, “The light curve simulation and its inversion problem for human-made space objects,” Ph.D. dissertation, Purdue University, Aug. 2020. DOI: [10.25394/PGS.12749570.v1](https://doi.org/10.25394/PGS.12749570.v1).
- [6] T. Schildknecht, R. Musci, and M. Fruh C. Ploner, “Color Photometry and Light Curve Observations of Space Debris in GEO,” in *Advanced Maui Optical and Space Surveillance Technologies Conference*, C. Paxson, H. Snell, J. Griffin, et al., Eds., Jan. 2008, E51, E51.
- [7] T. Schildknecht, N. Koshkin, E. Korobeinikova, et al., “Photometric Monitoring of Non-resolved Space Debris and Databases of Optical Light Curves,” in *Advanced Maui Optical and Space Surveillance Technologies Conference*, Jan. 2015, 25, p. 25.
- [8] A. Burton and S. Fan, “Mapping the solution space for light curve attitude estimation,” *43rd COSPAR Scientific Assembly. Held 28 January-4 February*, vol. 43, p. 2193, 2021.
- [9] H. Krag, “A method for the validation of space debris models and for the analysis and planning of radar and optical surveys,” Ph.D. dissertation, Technische Universität Braunschweig, Mar. 2003.
- [10] H. N. Russell, “On the light-variations of asteroids and satellites,” *The Astrophysical Journal*, vol. 24, no. 1, pp. 1–18, 1906.

- [11] M. Kaasalainen and J. Torppa, “Optimization methods for asteroid lightcurve inversion: I. shape determination,” *Icarus*, vol. 153, no. 1, pp. 24–36, 2001, ISSN: 0019-1035. DOI: <https://doi.org/10.1006/icar.2001.6673>. [Online]. Available: <https://www.sciencedirect.com/science/article/pii/S0019103501966734>.
- [12] M. Kaasalainen, J. Torppa, and K. Muinonen, “Optimization methods for asteroid lightcurve inversion: II. the complete inverse problem,” *Icarus*, vol. 153, no. 1, pp. 37–51, 2001, ISSN: 0019-1035. DOI: <https://doi.org/10.1006/icar.2001.6674>. [Online]. Available: <https://www.sciencedirect.com/science/article/pii/S0019103501966746>.
- [13] H. Minkowski, “Allgemeine lehrsätze über die konvexen polyeder,” in *Ausgewählte Arbeiten zur Zahlentheorie und zur Geometrie: Mit D. Hilberts Gedächtnisrede auf H. Minkowski, Göttingen 1909*. Springer Vienna, 1909, ch. 22, pp. 121–139. [Online]. Available: https://doi.org/10.1007/978-3-7091-9536-9_5.
- [14] J. J. Little, “An iterative method for reconstructing convex polyhedra from extended gaussian images,” in *Proceedings of the Third AAAI Conference on Artificial Intelligence*, ser. AAAI’83, Washington, D.C.: AAAI Press, 1983, pp. 247–250.
- [15] J. urech and M. Kaasalainen, “Photometric signatures of highly nonconvex and binary asteroids,” *Astronomy & Astrophysics*, vol. 404, no. 2, pp. 709–714, Jun. 2003. DOI: [10.1051/0004-6361:20030505](https://doi.org/10.1051/0004-6361:20030505).
- [16] C.-K. Chng, M. Sasdelli, and T.-J. Chin, “Globally optimal shape and spin pole determination with light-curve inversion,” *Monthly Notices of the Royal Astronomical Society*, vol. 513, no. 1, pp. 311–332, Jan. 2022, ISSN: 0035-8711. DOI: [10.1093/mnras/stac198](https://doi.org/10.1093/mnras/stac198). eprint: <https://academic.oup.com/mnras/article-pdf/513/1/311/43446894/stac198.pdf>. [Online]. Available: <https://doi.org/10.1093/mnras/stac198>.
- [17] J. Durech, V. Sidorin, and M. Kaasalainen, “DAMIT: a database of asteroid models,” *Astronomy and Astrophysics*, vol. 513, A46, A46, Apr. 2010. DOI: [10.1051/0004-6361/200912693](https://doi.org/10.1051/0004-6361/200912693).
- [18] M. Kaasalainen, J. urech, and V. Sidorin, *DAMIT: Database of Asteroid Models from Inversion Techniques*, Astrophysics Source Code Library, record ascl:1412.004, Dec. 2014. ascl: [1412.004](https://doi.org/10.1781/ascl.1412.004).
- [19] B. Calef, J. Africano, B. Birge, D. Hall, and P. Kervin, “Photometric signature inversion,” in *Unconventional Imaging II*, V. L. Gamiz, P. S. Idell, and M. S. Strojnik, Eds., International Society for Optics and Photonics, vol. 6307, SPIE, 2006, pp. 141–150. DOI: [10.1117/12.683015](https://doi.org/10.1117/12.683015). [Online]. Available: <https://doi.org/10.1117/12.683015>.

- [20] B. K. Bradley and P. Axelrad, “Lightcurve inversion for shape estimation of geo objects from space-based sensors,” in *Proceedings of the International Symposium on Space Flight Dynamics*, 2014, pp. 1–20.
- [21] S. Fan and C. Frueh, “A direct light curve inversion scheme in the presence of measurement noise,” *The Journal of the Astronautical Sciences*, vol. 67, Aug. 2019. DOI: [10.1007/s40295-019-00190-3](https://doi.org/10.1007/s40295-019-00190-3).
- [22] S. Fan and C. Frueh, “Multi-hypothesis light curve inversion scheme for convex objects with minimal observations,” in *Proceedings of the 8th European Conference on Space Debris*, ESA Space Debris Office, 2021, pp. 1–7.
- [23] A. M. Friedman, “Observability analysis for space situational awareness,” Ph.D. dissertation, Purdue University, Apr. 2020. DOI: [10.25394/PGS.12196863.v1](https://doi.org/10.25394/PGS.12196863.v1).
- [24] A. M. Friedman and C. Frueh, “Observability of light curve inversion for shape and feature determination exemplified by a case analysis,” *Journal of the Astronautical Sciences*, vol. 69, no. 2, pp. 537–569, Apr. 2022. DOI: [10.1007/s40295-021-00293-w](https://doi.org/10.1007/s40295-021-00293-w).
- [25] D. V. Cabrera, J. Utzmann, and R. Förstner, “Inversion of the shape of space debris from non-resolved optical measurements within spook,” in *Proceedings of the 22nd Advanced Maui Optical and Space Surveillance Technologies Conference*, 2021, pp. 1–18.
- [26] R. Linares, M. Jah, and J. Crassidis, “Inactive space object shape estimation via astrometric and photometric data fusion,” *Advances in the Astronautical Sciences*, vol. 143, pp. 217–232, Jan. 2012.
- [27] R. Linares, M. K. Jah, J. L. Crassidis, and C. K. Nebelecky, “Space object shape characterization and tracking using light curve and angles data,” *Journal of Guidance, Control, and Dynamics*, vol. 37, no. 1, pp. 13–25, 2014. DOI: [10.2514/1.62986](https://doi.org/10.2514/1.62986).
- [28] R. Linares and J. L. Crassidis, “Space-object shape inversion via adaptive hamiltonian markov chain monte carlo,” *Journal of Guidance, Control, and Dynamics*, vol. 41, no. 1, pp. 47–58, 2018.
- [29] R. Linares and R. Furfaro, “Space object classification using deep convolutional neural networks,” in *19th International Conference on Information Fusion*, Jul. 2016, pp. 1–8.

- [30] E. Kerr, G. P. Elisabeth, P. Talon, and D. Petit, “Using ai to analyse light curves for geo object characterisation,” in *Proceedings of the 22nd Advanced Maui Optical and Space Surveillance Technologies Conference*, 2021, pp. 1–9.
- [31] K. McNally, D. Ramirez, A. M. Anton, D. Smith, and J. Dick, “Artificial intelligence for space resident objects characterisation with lightcurves,” in *Proceedings of the 8th European Conference on Space Debris*, ESA Space Debris Office, 2021, pp. 1–12.
- [32] J. Allworth, L. Windrim, J. Bennett, and M. Bryson, “A transfer learning approach to space debris classification using observational light curve data,” *Acta Astronautica*, vol. 181, pp. 301–315, Jan. 2021. DOI: [10.1016/j.actaastro.2021.01.048](https://doi.org/10.1016/j.actaastro.2021.01.048).
- [33] S. Karpov, E. Katkova, G. Beskin, *et al.*, “Massive photometry of low-altitude artificial satellites on Mini-Mega-TORTORA,” in *Revista Mexicana de Astronomia y Astrofisica Conference Series*, ser. Revista Mexicana de Astronomia y Astrofisica Conference Series, vol. 48, Dec. 2016, pp. 112–113.
- [34] C. Benson, D. Scheeres, and N. Moskovitz, “Light curves of retired geosynchronous satellites,” in *7th European Conference on Space Debris*, vol. 7, 2017, p. 04.
- [35] N. Koshkin, L. Shakun, E. Korobeynikova, *et al.*, “Monitoring of space debris rotation based on photometry,” *Odessa Astronomical Publications*, vol. 31, pp. 179–185, 2018.
- [36] Y. Wang, X. Du, J. Zhao, Z. Yin, and Y. Song, “What causes the abrupt changes in the light curve of a geo satellite?” *Acta Astronautica*, vol. 153, pp. 130–137, 2018, ISSN: 0094-5765. DOI: <https://doi.org/10.1016/j.actaastro.2018.10.035>. [Online]. Available: <https://www.sciencedirect.com/science/article/pii/S0094576518313857>.
- [37] S. Fan, C. Frueh, and A. Buzzoni, “A light curve simulation of the apollo lunar ascent module,” in *AIAA/AAS Astrodynamics Specialist Conference*, 2016, pp. 1–10. DOI: [10.2514/6.2016-5504](https://doi.org/10.2514/6.2016-5504).
- [38] D. Kobayashi and C. Frueh, “Compressed sensing for satellite characterization,” in *Proceedings of the 20th AAS/AIAA Astrodynamics Specialist Conference*, Aug. 2020, pp. 1–20.
- [39] C. Früh and M. K. Jah, “Coupled orbit attitude motion of high area-to-mass ratio (hamr) objects including efficient self-shadowing,” *Acta Astronautica*, vol. 95, pp. 227–241, 2014, ISSN: 0094-5765. DOI: <https://doi.org/10.1016/j.actaastro.2013.11.017>.

- [40] J. Allworth, L. Windrim, J. Wardman, D. Kucharski, J. Bennett, and M. Bryson, “Development of a high fidelity simulator for generalised photometric based space object classification using machine learning,” in *Proceedings of 70th International Astronautical Congress*, International Astronautical Congress, 2019, pp. 1–14. DOI: [10.48550/ARXIV.2004.12270](https://doi.org/10.48550/ARXIV.2004.12270). [Online]. Available: <https://arxiv.org/abs/2004.12270>.
- [41] R. Furfaro, R. Linares, and V. Reddy, “Shape Identification of Space Objects via Light Curve Inversion Using Deep Learning Models,” in *Proceedings of the 20th Advanced Maui Optical and Space Surveillance Technologies Conference*, S. Ryan, Ed., Sep. 2019, 17, p. 17.
- [42] L. D. J. Blacketer, “Attitude characterisation of space objects using optical light curves,” Ph.D. dissertation, University of Southampton, Mar. 2022. [Online]. Available: <https://eprints.soton.ac.uk/457200/>.
- [43] C. J. Benson, D. J. Scheeres, W. H. Ryan, and E. V. Ryan, “Cyclic complex spin state evolution of defunct geo satellites,” in *Proceedings of the Advanced Maui Optical and Space Surveillance Technologies Conference, Maui, HI*, 2018.
- [44] F. L. Markley and J. L. Crassidis, *Fundamentals of Spacecraft Attitude Determination and Control*. Springer, May 2014.
- [45] M. D. Shuster, “Survey of attitude representations,” *Journal of the Astronautical Sciences*, vol. 41, no. 4, pp. 439–517, Oct. 1993.
- [46] P. Shirley and S. Marschner, *Fundamentals of Computer Graphics*, 3rd. USA: A. K. Peters, Ltd., 2009, ISBN: 1568814690.
- [47] D. Newell and E. Tiesinga, *The international system of units (si), 2019 edition*, en, Aug. 2019. DOI: <https://doi.org/10.6028/NIST.SP.330-2019>.
- [48] L. T. Sharpe, A. Stockman, W. Jagla, and H. Jägle, “A luminous efficiency function, $V^*(\lambda)$, for daylight adaptation,” *Journal of Vision*, vol. 5, no. 11, pp. 3–3, Dec. 2005, ISSN: 1534-7362. DOI: [10.1167/5.11.3](https://doi.org/10.1167/5.11.3). eprint: https://arvojournals.org/arvo/content/_public/journal/jov/932833/jov-5-11-3.pdf. [Online]. Available: <https://doi.org/10.1167/5.11.3>.
- [49] K. A. Pickering, “The Southern Limits of the Ancient Star Catalog and the Commentary of Hipparchos,” *DIO*, vol. 12, pp. 3–27, Sep. 2002.

- [50] F. Falchi, P. Cinzano, D. Duriscoe, *et al.*, *Supplement to: The new world atlas of artificial night sky brightness. v. 1.1. gfz data services.* <https://doi.org/10.5880/GFZ.1.4.2016.001>, Accessed: 2023-08-25, 2016.
- [51] F. Falchi, P. Cinzano, D. Duriscoe, *et al.*, “The new world atlas of artificial night sky brightness,” *Science Advances*, vol. 2, no. 6, e1600377, 2016. DOI: [10.1126/sciadv.1600377](https://doi.org/10.1126/sciadv.1600377). eprint: <https://www.science.org/doi/pdf/10.1126/sciadv.1600377>. [Online]. Available: <https://www.science.org/doi/abs/10.1126/sciadv.1600377>.
- [52] F. Patat, O. S. Ugolnikov, and O. V. Postylyakov, “UBVRI twilight sky brightness at ESO-Paranal,” *Astronomy and Astrophysics*, vol. 455, no. 1, pp. 385–393, Aug. 2006. DOI: [10.1051/0004-6361:20064992](https://doi.org/10.1051/0004-6361:20064992). arXiv: [astro-ph/0604128 \[astro-ph\]](https://arxiv.org/abs/astro-ph/0604128).
- [53] A. e. a. Vallenari, “Gaia Data Release 3. Summary of the content and survey properties,” *Astronomy & Astrophysics*, vol. 674, A1, A1, Jun. 2023. DOI: [10.1051/0004-6361/202243940](https://doi.org/10.1051/0004-6361/202243940). arXiv: [2208.00211 \[astro-ph.GA\]](https://arxiv.org/abs/2208.00211).
- [54] J. C. Segovia, *Astroquery.gaia package*, <https://astroquery.readthedocs.io/en/latest/gaia/gaia.html>, Accessed: 2023-08-21, 2016.
- [55] G. M. Daniels, “A night sky model for satellite search systems.,” *Optical Engineering*, vol. 16, pp. 66–71, Feb. 1977.
- [56] F. E. Roach, “A Photometric Model of the Zodiacal Light,” *Astronomical Journal*, vol. 77, p. 887, Dec. 1972. DOI: [10.1086/111363](https://doi.org/10.1086/111363).